TECHNISCHE MECHANIK, v32, 2-5, (2012), 463 – 483
submitted: November 1, 2011

Computational Mesoscale Modeling and Homogenization of Liquid-Phase Sintering of Particle Agglomerates

M. Öhman, K. Runesson, F. Larsson

Liquid phase sintering of particle agglomerates is simulated as the viscous deformation due to particle-particle contact, whereby the single driving force is the surface tension on the particle/pore interface. Particles are modeled as purely viscous fluids (with no elasticity). Computational homogenization is adopted for the RVE with Dirichlet boundary conditions. A surface motion algorithm was developed that requires complete remeshing of the FE-mesh based on a maximum deformation criterion. Since the particles are intrinsically incompressible, the macroscopic compressibility is determined from shrinking porosity in the substructure. The numerical examples include free sintering of an RVE and a fully coupled FE^2-simulation of a specimen with inhomogeneous initial distribution of porosity.

1 Introduction

To model and simulate in quantitative terms the sintering process in a powder after cold compaction and the subsequent heating is a classical task in material mechanics. For a hardmetal (such as WC-Co) the binder metal Co is heated to melt in order to obtain sufficient mobility via capillary action, i.e. via surface traction, stemming from stored surface energy. The resulting flow causes gradual filling of the pore space and brings about a macroscopic shrinkage of the particle compact until a completely dense state is obtained, at least ideally. The engineering task is to (i) estimate the final resulting quality (i.e. in terms of porosity) and (ii) to predict the final net shape and size of the sintered component.

A wealth of literature has been devoted to the modeling and simulation of the sintering process. From a mesoscale viewpoint, a classical approach is to consider so-called unit problems, whereby the constitutive modeling is based on diffusion and, most importantly, flow models. Since the literature is abundant, it is not our aim to give a comprehensive review. We shall rather focus our brief review on work devoted to computational modeling and simulation. Among the early attempts to numerically simulate the surface-tension driven reshaping of contacting particles are those by Jagota and Dawson (1988a,b), van de Vorst (1993). In a series of papers, Zhou and Derby (2001, 1998) emphasize efficient finite element algorithms to trace the complex 3-dimensional flow of multi-particle interaction. The main challenges are the complex subscale geometry and the moving free boundary giving rise to very large deformations and severe topology changes. Recent developments of free-boundary tracing FE-strategies for large deformations (without severe topological changes) are discussed by Dettmer and Perić (2006), Saksono and Perić (2006a,b). All the mentioned work consider surface tension effects in fluids. A recent extension to include surface tension in the context of solid modeling, where anisotropic surface energy may be present, is due to Javili and Steinmann (2010, 2009).

Attempts have also been made in the literature to use macroscopic models based on nonlinear viscoelasticity and viscoplasticity. In such models the densification process is driven by the sintering stress, which is the macroscale manifestation of the stored surface energy. From a thermodynamical viewpoint, it is the dissipative stress that is conjugated to the current macroscale porosity, e.g. Mähler and Runesson (2000), Reid and Oakberg (1990). Among the literature on macroscale modeling, we mention Lu et al. (2001), Svoboda et al. (1996) and Xu and Mehrabadi (1997).

In this paper we consider the generic problem of homogeneous particles which deform as a viscous fluid with sufficiently high viscosity to motivate the neglect of all acceleration terms. Hence, it is proposed to use a non-linear Stokes formulation to model the creeping flow of the melt-phase within the Representative Volume Element (RVE). The simplifying assumption is introduced that the flow properties are unaffected by temperature changes, i.e the

sintering process is only modeled during the fully heated part of the process. The process is simulated from initial porosity to a dense product, at which stage the surface tension effects have disappeared. However, due to possible initially inhomogeneous porosity in the green body, a remaining macroscopic distortion may be present (macroscale deviatoric deformation superimposed on the volume change).

The paper is structured as follows: The various features of subscale modeling (surface tension, particle arrangements within the RVE, etc.) are presented in Section 3. This is followed in Section 4 by the description of the macroscale problem, whereas the RVE-problem with Dirichlet boundary conditions is presented in Section 5. The next sections contain algorithmic features and numerical examples based on a single RVE as well as FE^2-computations. Conclusions and an outlook to future developments are given in the final section.

2 Notation

Square brackets are used for defining the syntactic structure of expressions. Parentheses are used to denote explicit functional dependence on its arguments, whereas curly brackets are used to denote implicit functions. A semicolon is used to delimit nonlinear and linear arguments in variational forms, e.g. $a(\boldsymbol{u};\boldsymbol{v})$ means that a is nonlinear in $\boldsymbol{u}$, whereas it is linear in $\boldsymbol{v}$.

3 Subscale Modeling

3.1 Preliminaries

We consider a sintering body with current macroscale configuration $\Omega(t)$ in space for any given time $t \geq 0$. Our aim is to exploit the concept of computational homogenization in order to determine the unknown $\Omega(t)$ and certain mechanical fields on $\Omega(t)$, such as the current macroscale velocity field, $\bar{\boldsymbol{v}}$, the macroscale true stress field, $\bar{\boldsymbol{\sigma}}$, and the macroscale porosity field, $\bar{\Phi}(t)$. We note that the initial configuration $\Omega(0)$ represents the so called green body, obtained after cold compaction and characterized by the inhomogeneous (macroscopic) porosity $\bar{\Phi}(t=0)$. In the case of free sintering, i.e. sintering without any external loading, it is clear that $\bar{\boldsymbol{\sigma}}$ represents the macroscopic residual stresses at every instant in time. Subsequently, we shall adopt modeling on the subscale in terms of creeping fluid flow, which means that it will be possible to trace the development of the current macroscale configuration $\Omega(t)$ by computing the macroscale velocity field $\bar{\boldsymbol{v}}(\bar{\boldsymbol{x}},t)$ for $(\bar{\boldsymbol{x}},t) \in \Omega \times (0,T)$.

In a 3D representation of the microstructure the assembly of sintering particles create an open pore system (at least initially), and the morphology of the pore space can be quite complex with a large number of inter-particle contact surfaces that evolve with time during the sintering process and possibly thereafter due to creep (when the temperature is reduced to the ambient one). With reasonable accuracy one may then assume that the pore surfaces are free surfaces, i.e. the pore gas does not impose any resistance on the motion. The situation is, of course, different in the (physically unrealistic) case of a 2D representation of the microstructure. The pore system will then inevitably be closed from the start of the sintering process, and the trapped gas may impose a pressure on the pore surfaces that require a constitutive assumption. In any case the pertinent surfaces associated with surface tension are particle/pore and particle/particle (contact) surfaces, as indicated in Figure 1.

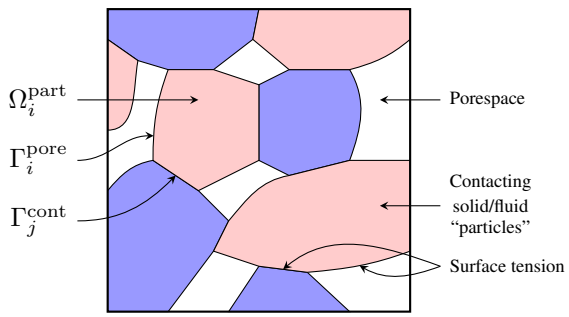

Figure 1: Microstructure of porous particulate material with sintering particles in contact. The colors indicate particles with different constitutive behavior and surface energies.

3.2 Surface Tension

The surface tension along particle/particle and particle/pore interfaces (the latter denoted pore boundaries) is considered to be the sole driving force of the sintering process, and it is defined in terms of a surface tension force $\hat{\boldsymbol{t}}$ acting in the tangent plane of the surface. In the simplest (and most common) case of isotropic surface tension, this traction is characterized by the constant surface-specific surface energy γ_{s} in the current configuration as the single material parameter. Although we adopt this simplified model below in the numerical results, it is illuminating to consider the more general situation of anisotropic surface stress that may also depend on the surface deformation via a suitable constitutive assumption, cf. Steinmann (2008).

We shall next establish the equilibrium equations that are pertinent to the presence of surface tension. These relate to (i) smooth surface segments (external boundaries or interfaces) and (ii) curves that represent the intersection of two (or more) surfaces. The analysis is restricted to quasistatic conditions and the spatial (Eulerian) description. For the purpose of illustration, we shall refer to the 2D-situation shown in Figure 2 of two contacting particles surrounded by pore space. The contact interface is assumed to be smooth, whereas the outer surfaces are assumed piecewise smooth. Hence, we allow for a possible kink (sharp corner) at point α and a triple junction at point β (for the purpose of generality). Hence each *smooth* surface (interface) segment Γ_i, for $i = 1, \dots, M_{\mathrm{segm}}$, has a continuously varying normal, $\boldsymbol{n}$. Moreover, the binormal at each end-point is denoted $\boldsymbol{m}$. The binormal is defined as the vector orthogonal to both the surface normal and the edge tangent, positive out from the surface, as illustrated in Figure 3. For example, in Figure 2, the binormals of the segment Γ_2 are denoted $\boldsymbol{m}_\alpha^{(2)}$ and $\boldsymbol{m}_\beta^{(2)}$. In the general 3D-situation of a smooth space-curved surface Γ, the binormal $\boldsymbol{m}$ is normal to the enclosing smooth space-curve $\partial\Gamma$ and lies in the tangential plane of Γ. In particular, $\boldsymbol{m}$ is orthogonal to the surface normal $\boldsymbol{n}$.

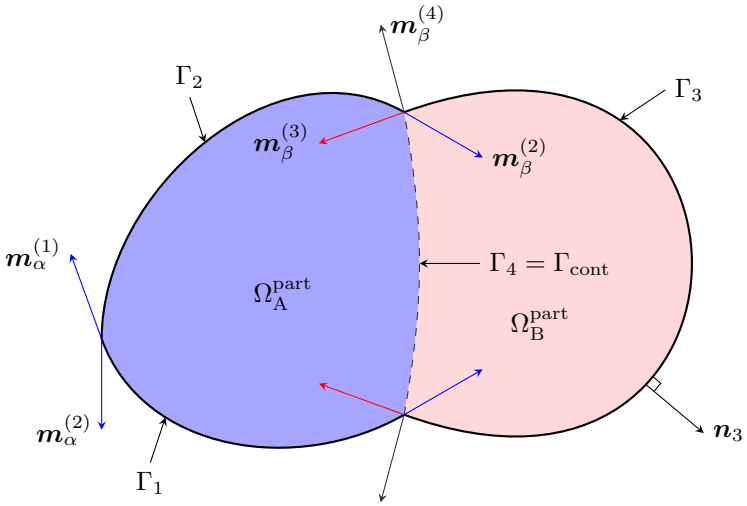

Figure 2: Illustration in 2D of two contacting particles along a smooth interface and with piecewise smooth free surfaces.

The smooth space-curved surface segment Γ, as shown in Figure 3, is considered as a thin shell acted upon by the tractions $\boldsymbol{t}^+$ and $\boldsymbol{t}^-$ on the upper and lower sides. These tractions are part of the final solution in the case Γ is the contact interface of two bodies (solid or fluid) with different material properties. When Γ is an outer surface, then $\boldsymbol{t}^+$ represents a prescribed loading (or reaction from prescribed displacement), whereas $-\boldsymbol{t}^-$ is the traction acting on the material just below the surface. In addition, the surface tension force $\hat{\boldsymbol{t}}$ acts in the tangent plane of the thin shell. Equilibrium is expressed as

$$\int_\Gamma \left[\boldsymbol{t}^+ + \boldsymbol{t}^-\right] \mathrm{d}a = \int_{\partial\Gamma} \hat{\boldsymbol{t}}\, \mathrm{d}l = \boldsymbol{0} \tag{1}$$

Upon introducing the surface stress tensor $\hat{\boldsymbol{\sigma}}$ (with components only in the tangent plane), such that $\hat{\boldsymbol{t}} = \hat{\boldsymbol{\sigma}} \cdot \boldsymbol{m}$ and $\hat{\boldsymbol{\sigma}} \cdot \boldsymbol{n} = \boldsymbol{0}$, we may use the surface divergence theorem for a smooth surface segment to rephrase the curve integral in (1) as

$$\int_{\partial\Gamma} \hat{\boldsymbol{\sigma}} \cdot \boldsymbol{m}\, \mathrm{d}l = \int_\Gamma \hat{\boldsymbol{\sigma}} \cdot \hat{\boldsymbol{\nabla}}\, \mathrm{d}a + \int_\Gamma \kappa \hat{\boldsymbol{\sigma}} \cdot \boldsymbol{n}\, \mathrm{d}a = \int_\Gamma \hat{\boldsymbol{\sigma}} \cdot \hat{\boldsymbol{\nabla}}\, \mathrm{d}a \tag{2}$$

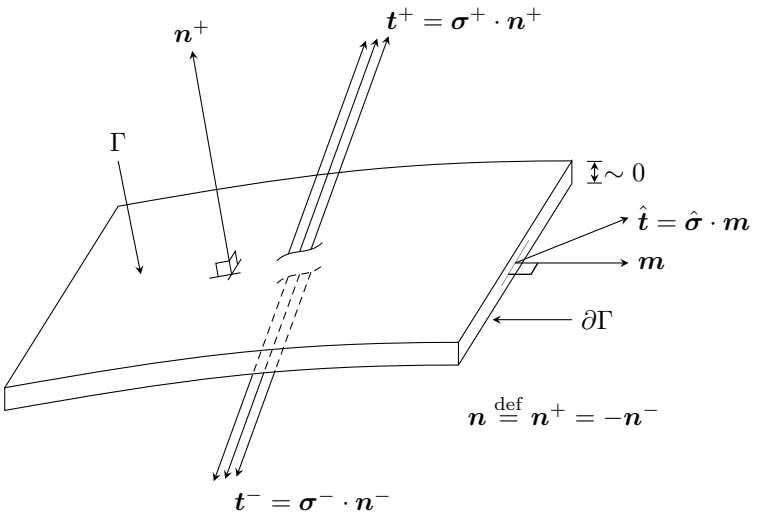

Figure 3: Thin shell representing a surface with in-plane forces due to surface tension.

Here, $\hat{\boldsymbol{\nabla}} \stackrel{\text{def}}{=} \boldsymbol{\nabla} - [\boldsymbol{\nabla} \cdot \boldsymbol{n}]\boldsymbol{n}$ is the surface gradient operator, $\boldsymbol{\nabla}$ is the spatial gradient operator, $\kappa \stackrel{\text{def}}{=} \boldsymbol{n} \cdot \hat{\boldsymbol{\nabla}}$ is the curvature and $\boldsymbol{n} \stackrel{\text{def}}{=} \boldsymbol{n}^+$ is taken positive outwards from a convex surface. Combining (1) and (2) and localizing the result for any arbitrary choice of Γ, we obtain the strong format of traction equilibrium as follows

$$\boldsymbol{t}^+ + \boldsymbol{t}^- + \boldsymbol{t}_{\mathrm{s}} = \boldsymbol{0} \quad \text{on } \Gamma \quad \text{with } \boldsymbol{t}_{\mathrm{s}} \stackrel{\text{def}}{=} \hat{\boldsymbol{\sigma}} \cdot \hat{\boldsymbol{\nabla}} \tag{3}$$

where $\boldsymbol{t}_{\mathrm{s}}$ is the surface tension traction. Since it can be shown that $\boldsymbol{t}_{\mathrm{s}}$ will depend on the (local) curvature, it is well-defined only when Γ is sufficiently smooth.

Next, assume that boundary parts of the smooth surfaces coincide along the space curve $\mathcal{C} = \cap_i \partial\Gamma_i$. Denoting the corresponding binormals by $\boldsymbol{m}_i$ (which are all normals to $\mathcal{C}$), we obtain the equilibrium condition

$$\sum_i \hat{\boldsymbol{t}}_i = \sum_i \hat{\boldsymbol{\sigma}}_i \cdot \boldsymbol{m}_i = \boldsymbol{0} \quad \text{on } \mathcal{C} \tag{4}$$

Special case: Isotropic surface tension

Consider the special case that the surface tension is isotropic and homogeneous in the spatial format, i.e. $\hat{\boldsymbol{\sigma}} = \gamma_{\mathrm{s}} \hat{\boldsymbol{I}}$, where γ_{s} is a constant parameter and $\hat{\boldsymbol{I}} \stackrel{\text{def}}{=} \boldsymbol{I} - \boldsymbol{n} \otimes \boldsymbol{n}$ is the surface identity tensor. Using the identity $\hat{\boldsymbol{I}} \cdot \hat{\boldsymbol{\nabla}} = -\kappa \boldsymbol{n}$, we then obtain

$$\boldsymbol{t}_{\mathrm{s}} \stackrel{\text{def}}{=} -\kappa \gamma_{\mathrm{s}} \boldsymbol{n} \quad \text{on } \Gamma, \quad \hat{\boldsymbol{t}}_i = \gamma_{\mathrm{s},i} \boldsymbol{m}_i \quad \text{on } \mathcal{C} \tag{5}$$

As an example, consider the situation in Figure 2, where $\Gamma_1, \Gamma_2, \Gamma_3$ represent (free) pore surfaces, whereas Γ_4 represents the interface along which two particles occupying $\Omega_{\mathrm{A}}^{\mathrm{part}}$ and $\Omega_{\mathrm{B}}^{\mathrm{part}}$ are in contact. The relevant surface tension parameters are $\gamma_{\mathrm{s,A}}, \gamma_{\mathrm{s,B}}$ and $\gamma_{\mathrm{s,AB}}$.

For surfaces Γ_1 and Γ_2, we obtain: $\boldsymbol{t}^+ = \boldsymbol{0}, \boldsymbol{t}^- = -\boldsymbol{\sigma} \cdot \boldsymbol{n} \stackrel{\text{def}}{=} -\boldsymbol{t}$ whereby (3) gives $\boldsymbol{t} = \boldsymbol{t}_{\mathrm{s,A}} = -\kappa \gamma_{\mathrm{s,A}} \boldsymbol{n}$. Likewise, for surface Γ_3, we obtain: $\boldsymbol{t} = \boldsymbol{t}_{\mathrm{s,B}} = -\kappa \gamma_{\mathrm{s,B}} \boldsymbol{n}$. For the interface Γ_4, we obtain: $\boldsymbol{t}^+ = \boldsymbol{\sigma}_{\mathrm{B}} \cdot \boldsymbol{n}$, $\boldsymbol{t}^- = -\boldsymbol{\sigma}_{\mathrm{A}} \cdot \boldsymbol{n}$, whereby (3) gives $[\boldsymbol{\sigma}_{\mathrm{A}} - \boldsymbol{\sigma}_{\mathrm{B}}] \cdot \boldsymbol{n} = -\kappa \gamma_{\mathrm{s,AB}} \boldsymbol{n}$.

As to the singular points, force balance at the kink at point $\boldsymbol{x}_\alpha$ requires

$$\hat{\boldsymbol{t}}_\alpha^{(1)} + \hat{\boldsymbol{t}}_\alpha^{(2)} = \gamma_{\mathrm{s,A}} \left[\boldsymbol{m}_\alpha^{(1)} + \boldsymbol{m}_\alpha^{(2)} \right] = \boldsymbol{0} \tag{6}$$

whereas force balance at the triple junction at point $\boldsymbol{x}_\beta$ requires

$$\hat{\boldsymbol{t}}_\beta^{(2)} + \hat{\boldsymbol{t}}_\beta^{(3)} + \hat{\boldsymbol{t}}_\beta^{(4)} = \gamma_{\mathrm{s,A}} \boldsymbol{m}_\beta^{(2)} + \gamma_{\mathrm{s,B}} \boldsymbol{m}_\beta^{(3)} + \gamma_{\mathrm{s,AB}} \boldsymbol{m}_\beta^{(4)} = \boldsymbol{0} \tag{7}$$

3.3 Incompressible Viscous Flow of the Stokes' Type

We shall adopt a model for the subscale deformation within the solid particles undergoing the time-dependent sintering process. The model is simplified in the sense that elastic deformation is neglected a priori. It is then possible to consider a viscoplastic (fluid-like) material with intrinsic incompressibility (within the particles). Such incompressibility is expressed as $d_{\mathrm{vol}} \overset{\mathrm{def}}{=} \boldsymbol{v} \cdot \boldsymbol{\nabla} = 0$ and, hence,

$$\boldsymbol{d}_{\mathrm{dev}} \overset{\mathrm{def}}{=} \boldsymbol{d} - \frac{1}{3} d_{\mathrm{vol}} \boldsymbol{I} = \boldsymbol{d} \overset{\mathrm{def}}{=} [\boldsymbol{v} \otimes \boldsymbol{\nabla}]^{\mathrm{sym}} \tag{8}$$

An isotropic and associated viscoplastic flow rule of the classical Perzyna type is proposed in the following restricted fashion

$$\boldsymbol{d} = \boldsymbol{d}_{\mathrm{dev}} = \frac{1}{2\mu} \boldsymbol{\sigma}_{\mathrm{dev}} + \boldsymbol{d}^{\mathrm{p}}_{\mathrm{dev}}(\boldsymbol{\sigma}_{\mathrm{dev}}), \quad \boldsymbol{d}^{\mathrm{p}}_{\mathrm{dev}} = \frac{1}{t_*} \eta \left(\Phi \left(\sigma_{\mathrm{e}} \right) \right) \frac{\mathrm{d}\, \Phi}{\mathrm{d} \boldsymbol{\sigma}} \tag{9}$$

where t_* is the relaxation time, $\eta(\Phi)$ is an overstress function, $\Phi(\sigma_{\mathrm{e}})$ is the quasistatic yield function and $\sigma_{\mathrm{e}} = \sqrt{\frac{3}{2}} |\boldsymbol{\sigma}_{\mathrm{dev}}|$ is the equivalent stress. Upon introducing the abbreviated notation $k = \frac{\eta}{t_*} \frac{\mathrm{d}\, \Phi}{\mathrm{d} \sigma_{\mathrm{e}}}$, we may solve for σ_{e} in terms of the equivalent rate of deformation $d_{\mathrm{e}} \overset{\mathrm{def}}{=} \sqrt{\frac{2}{3}} |\boldsymbol{d}_{\mathrm{dev}}|$ from the equation

$$\frac{1}{3\mu} \sigma_{\mathrm{e}} + k \left(\sigma_{\mathrm{e}} \right) = d_{\mathrm{e}} \tag{10}$$

and we, finally, obtain the Newtonian-like constitutive relation

$$\boldsymbol{\sigma}_{\mathrm{dev}}(\boldsymbol{d}) = 2 \tilde{\mu} \boldsymbol{d}_{\mathrm{dev}}, \quad \tilde{\mu} \overset{\mathrm{def}}{=} \frac{\sigma_{\mathrm{e}}}{3 d_{\mathrm{e}}} \tag{11}$$

The corresponding tangent stiffness $\mathsf{E}_{\mathrm{T,dev}}$ in the relation $\mathrm{d} \boldsymbol{\sigma}_{\mathrm{dev}} = \mathsf{E}_{\mathrm{T,dev}} : \mathrm{d} \boldsymbol{d}$ (representing the linearization of the subscale constitutive problem), is given as follows:

$$\mathsf{E}_{\mathrm{T,dev}} = 2 \tilde{\mu} \mathbf{I}_{\mathrm{dev}} + \frac{4}{9 d_{\mathrm{e}}^2} \left[d_{\mathrm{e}} \left[\frac{1}{3\mu} + k' \right]^{-1} - \sigma_{\mathrm{e}} \right] \boldsymbol{d}_{\mathrm{dev}} \otimes \boldsymbol{d}_{\mathrm{dev}} \tag{12}$$

with

$$k' = \frac{1}{t_*} \left[\eta \frac{\mathrm{d}^2\, \Phi}{\mathrm{d} \sigma_{\mathrm{e}}^2} + \frac{\mathrm{d}\, \eta}{\mathrm{d} \Phi} \left[\frac{\mathrm{d}\, \Phi}{\mathrm{d} \sigma_{\mathrm{e}}} \right]^2 \right]. \tag{13}$$

In the absence of acceleration, the balance equations for the quasi-static motion of the viscoplastic particles can be established in the spatial setting as follows

$$-\boldsymbol{\sigma} \cdot \boldsymbol{\nabla} = \boldsymbol{0} \quad \text{in } \Omega^{\mathrm{part}}_i \quad i = 1, 2, ... \tag{14a}$$

$$\boldsymbol{v} \cdot \boldsymbol{\nabla} = 0 \quad \text{in } \Omega^{\mathrm{part}}_i \tag{14b}$$

where $\boldsymbol{\sigma}(\boldsymbol{d}) = \boldsymbol{\sigma}_{\mathrm{dev}}(\boldsymbol{d}) - p \boldsymbol{I}$ is the total Cauchy stress, p is the pressure (Lagrangian multiplier corresponding to the incompressibility constraint), and where $\boldsymbol{\nabla}$ denotes the spatial gradient.

Referring to Figure 1, we consider the collection of particles inside Ω. Each particle domain Ω^{part}_i has part of its boundary associated with the pore surface Γ^{pore}_i. In addition, two particles are in contact across the surface Γ^{cont}_j. We also introduce the notation $\Omega^{\mathrm{part}} \overset{\mathrm{def}}{=} \cup_i \Omega^{\mathrm{part}}_i$, $\Gamma^{\mathrm{pore}} \overset{\mathrm{def}}{=} \cup_i \Gamma^{\mathrm{pore}}_i$ and $\Gamma^{\mathrm{cont}} \overset{\mathrm{def}}{=} \cup_j \Gamma^{\mathrm{cont}}_j$. Furthermore we introduce $\Gamma^{\mathrm{part,ext}}$ which denotes the intersection of the boundary of Ω^{part} and the external boundary of the considered domain Ω, denoted Γ^{ext}, where a there may be a prescribed external force $\boldsymbol{t}_{\mathrm{p}}$. It can then be shown that the weak form of (14) are

$$\int_{\Omega^{\mathrm{part}}} \boldsymbol{\sigma} : [\delta \boldsymbol{v} \otimes \boldsymbol{\nabla}] \, \mathrm{d}v = - \int_{\Gamma^{\mathrm{pore}} \cup \Gamma^{\mathrm{cont}}} \hat{\boldsymbol{\sigma}} : \left[\delta \boldsymbol{v} \otimes \hat{\boldsymbol{\nabla}} \right] \mathrm{d}a + \int_{\Gamma^{\mathrm{part,ext}}} \boldsymbol{t}_{\mathrm{p}} \cdot \delta \boldsymbol{v} \, \mathrm{d}a \tag{15a}$$

$$\int_{\Omega^{\mathrm{part}}} [\boldsymbol{v} \cdot \boldsymbol{\nabla}] \, \delta p \, \mathrm{d}v = 0 \tag{15b}$$

for suitable test functions $\delta\boldsymbol{v}$ and δp that satisfy the appropriate regularity requirements (not further elaborated in this paper).

In the special case of isotropic surface tension (not necessarily state-independent or homogeneous), we obtain the more explicit expression for the integral in (15a) that represents surface tension loading

$$\int_{\Gamma^{\mathrm{pore}}\cup\Gamma^{\mathrm{cont}}} \hat{\boldsymbol{\sigma}} : \left[\delta\boldsymbol{v}\otimes\hat{\boldsymbol{\nabla}}\right] \mathrm{d}a = \int_{\Gamma^{\mathrm{pore}}\cup\Gamma^{\mathrm{cont}}} \gamma_{\mathrm{s}} \left[\delta\boldsymbol{v}\cdot\hat{\boldsymbol{\nabla}}\right] \mathrm{d}a \tag{16}$$

In order to show (15a), we proceed in standard fashion by first multiplying (14a) with the test function $\delta\boldsymbol{v}$ and integrating on Ω_i^{part}, $i=1,2,...$, then integrating by parts while using the divergence theorem (in standard fashion). For a smooth pore surface segment Γ_i^{pore}, bounded by the curve $\partial\Gamma_i^{\mathrm{pore}}$, we next use the surface divergence theorem to reformulate the virtual work from tractions $\boldsymbol{t}$ as follows

$$\int_{\Gamma_i^{\mathrm{pore}}} \boldsymbol{t}\cdot\delta\boldsymbol{v}\,\mathrm{d}a = -\int_{\Gamma_i^{\mathrm{pore}}} \hat{\boldsymbol{\sigma}} : \left[\delta\boldsymbol{v}\otimes\hat{\boldsymbol{\nabla}}\right] \mathrm{d}a + \int_{\partial\Gamma_i^{\mathrm{pore}}} \hat{\boldsymbol{t}}\cdot\delta\boldsymbol{v}\,\mathrm{d}l. \tag{17}$$

Similarly, for a smooth contact surface segment Γ_j^{cont}, we obtain

$$\int_{\Gamma_j^{\mathrm{cont}}} \left[\boldsymbol{t}^+ + \boldsymbol{t}^-\right]\cdot\delta\boldsymbol{v}\,\mathrm{d}a = -\int_{\Gamma_j^{\mathrm{cont}}} \hat{\boldsymbol{\sigma}} : \left[\delta\boldsymbol{v}\otimes\hat{\boldsymbol{\nabla}}\right] \mathrm{d}a + \int_{\partial\Gamma_j^{\mathrm{cont}}} \hat{\boldsymbol{t}}\cdot\delta\boldsymbol{v}\,\mathrm{d}l. \tag{18}$$

Now, collecting the curve integrals, we obtain

$$\begin{aligned}
&\sum_i \int_{\partial\Gamma_i^{\mathrm{pore}}} \hat{\boldsymbol{t}}\cdot\delta\boldsymbol{v}\,\mathrm{d}l + \sum_j \int_{\partial\Gamma_j^{\mathrm{cont}}} \hat{\boldsymbol{t}}\cdot\delta\boldsymbol{v}\,\mathrm{d}l = \\
&\sum_\alpha \int_{\mathcal{C}_\alpha} \sum_\beta \hat{\boldsymbol{t}}_{\alpha\beta}\cdot\delta\boldsymbol{v}_\alpha\,\mathrm{d}l = \sum_\alpha \int_{\mathcal{C}_\alpha} \left[\sum_\beta \hat{\boldsymbol{t}}_{\alpha\beta}\right]\cdot\delta\boldsymbol{v}_\alpha\,\mathrm{d}l = 0
\end{aligned} \tag{19}$$

where we used the relation (4) to conclude the tension force balance $\sum_\beta \hat{\boldsymbol{t}}_{\alpha\beta} = \boldsymbol{0}$ along each curve $\mathcal{C}_\alpha$ that represent a kink along the pore surface or an intersection between two contacting particles and the pore space.

3.4 Representative Volume Element

An appropriately chosen RVE is assumed to occupy the bulk volume $\Omega_\square(t)$. The RVE must obviously contain a sufficient number of particles and pores to qualify as representative in the classical sense; however, in order to simplify the subsequent conceptual discussion and pave the way for the subsequent homogenization, we shall henceforth restrict the analysis to 2D, and we consider a simple arrangement of particles within the RVE. In the very simplest case that the RVE consists of one single unit cell containing a single contiguous pore in the 2D-projection.

The current bulk domain of the RVE at a time $t>0$ contains the particles and the pore space, $\Omega_\square(t) = \Omega_\square^{\mathrm{part}}(t) \cup \Omega_\square^{\mathrm{pore}}(t)$, where $\Omega_\square^{\mathrm{pore}}(t)$ is the domain currently occupied by the pore, whereas $\Omega_\square^{\mathrm{part}}(t)$ is occupied by the particles. This is shown schematically in Figure 4b. The external boundary of the RVE is $\partial\Omega_\square(t) \stackrel{\mathrm{def}}{=} \Gamma_\square(t)$. The initial configuration of the particles within the RVE (before any deformation has taken place) is denoted $\Omega_\square(0)$, as shown in Figure 4a. It is noted that in 2D, by assumption, the external boundary of the RVE always cuts through the particles and never through the pore space. The boundaries of the (closed) pore-space are collectively denoted $\Gamma_\square^{\mathrm{pore}}(t)$. For simplicity (but without loosing generality of the formulation), we shall henceforth ignore contributions from interfaces between contacting particles. The boundary of the deforming particles currently contained in the RVE is then $\partial\Omega_\square^{\mathrm{part}}(t) = \Gamma_\square(t) \cup \Gamma_\square^{\mathrm{pore}}(t)$.

4 Macroscale Problem

4.1 Macro- and Subscale Coupling — Variational Multiscale Setting

Classical model-based homogenization for a single-phase medium (without pores) is based on the virtual work equation that is volume-averaged on the Representative Volume Element (RVE). Such a strategy can be formulated

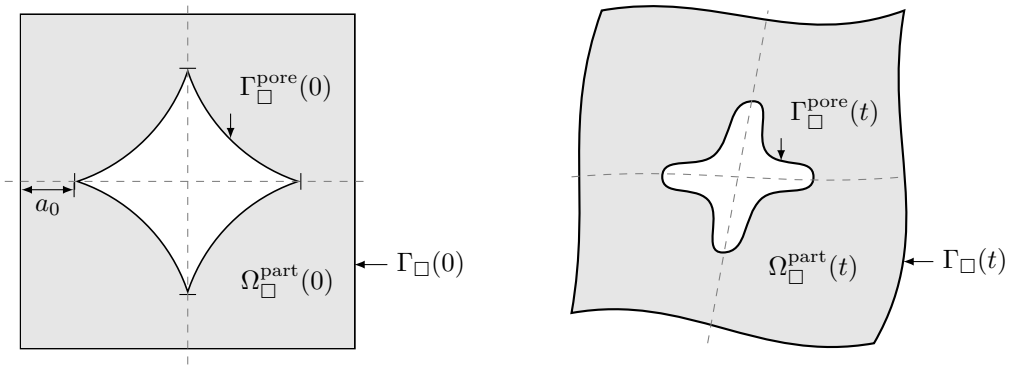

(a) $t = 0$ (b) $t > 0$

Figure 4: (a) Initial configuration of RVE in 2D consisting of circular particles in a perfect square lattice. The contact points are flattened due to precompaction. (b) Deformed configuration (sketchy).

in the spirit of the Variational Multiscale Method (VMM), c.f. Hughes et al. (1998), Larson and Må lqvist (2007). In the present case, when the virtual work equation (14a) is complemented by the constraint equation (14b), it is necessary to carefully consider the steps in VMM to arrive at the appropriate homogenized equation(s). To this end, we first introduce the abbreviated notation $z = (\boldsymbol{v}, p) \in \mathbb{Z} = \mathbb{V} \times \mathbb{P}$, where $\mathbb{Z}$ represents the space of fine-scale (non-homogenized) solutions to the system (15), which may conveniently be abbreviated in abstract form as the residual equation

$$R(z; \delta z) = 0 \quad \forall\, \delta z \in \mathbb{Z}^0 \tag{20}$$

where $\mathbb{Z}^0 = \mathbb{V}^0 \times \mathbb{P}$ is the test space and where each $\boldsymbol{v} \in \mathbb{V}^0$ vanishes on the Dirichlet part of $\Gamma^{\text{part,ext}}$. More explicitly, (20) can be rephrased as $R(z; \delta z) = R^{\text{v}}(\boldsymbol{v}, p; \delta \boldsymbol{v}) + R^{\text{p}}(\boldsymbol{v}, \delta p)$, where the two separate residual equations are defined as

$$R^{\text{v}}(\boldsymbol{v}, p; \delta \boldsymbol{v}) \stackrel{\text{def}}{=} l(\delta \boldsymbol{v}) - a(\boldsymbol{v}; \delta \boldsymbol{v}) - b(p, \delta \boldsymbol{v}) = 0 \quad \forall\, \delta \boldsymbol{v} \in \mathbb{V}^0 \tag{21a}$$

$$R^{\text{p}}(\boldsymbol{v}, \delta p) \quad \stackrel{\text{def}}{=} -b(\delta p, \boldsymbol{v}) \qquad\qquad = 0 \quad \forall\, \delta p \in \mathbb{P} \tag{21b}$$

where

$$a(\boldsymbol{v}; \delta \boldsymbol{v}) \stackrel{\text{def}}{=} \int_{\Omega^{\text{part}}} \boldsymbol{\sigma}_{\text{dev}}(\boldsymbol{d}) : [\delta \boldsymbol{v} \otimes \boldsymbol{\nabla}] \, \mathrm{d}v \tag{22}$$

$$b(p, \boldsymbol{v}) \quad \stackrel{\text{def}}{=} -\int_{\Omega^{\text{part}}} [\boldsymbol{v} \cdot \boldsymbol{\nabla}] p \, \mathrm{d}v \tag{23}$$

$$l(\delta \boldsymbol{v}) \quad \stackrel{\text{def}}{=} \int_{\Gamma^{\text{pore}}} \hat{\boldsymbol{\sigma}} : [\delta \boldsymbol{v} \otimes \hat{\boldsymbol{\nabla}}] \, \mathrm{d}a + \int_{\Gamma^{\text{part,ext}}} \boldsymbol{t}_{\text{p}} \cdot \delta \boldsymbol{v} \, \mathrm{d}a \tag{24}$$

Clearly, free sintering is defined by the situation $\boldsymbol{t}_{\text{p}} = \boldsymbol{0}$, such that the second integral in (24) vanishes. To simplify notation and avoid subtleties in defining homogenization of external boundary loads, this simplification will be adopted henceforth (without obscuring the generality of the proposed homogenization strategy).

A multiscale formulation of (20) is defined by the hierarchical split $\mathbb{Z} = \mathbb{Z}^{\text{M}} \oplus \mathbb{Z}^{\text{s}}$, where $\mathbb{Z}^{\text{M}}$ contains smooth macroscale functions and $\mathbb{Z}^{\text{s}}$ is the hierarchical complement of $\mathbb{Z}^{\text{M}}$ that, typically, represents the fine-scale features. It is assumed that each $z \in \mathbb{Z}$ can be split uniquely as $z = z^{\text{M}} + z^{\text{s}}$ such that $z^{\text{M}} \in \mathbb{Z}^{\text{M}}$ and $z^{\text{s}} \in \mathbb{Z}^{\text{s}}$. Therefore, solve $z^{\text{M}} \in \mathbb{Z}^{\text{M}}$, $z^{\text{s}} \in \mathbb{Z}^{\text{s}}$ such that (20) can be represented by the set of equations

$$R(z^{\text{M}} + z^{\text{s}}; \delta z^{\text{M}}) = 0 \quad \forall\, \delta z^{\text{M}} \in \mathbb{Z}^{\text{M},0} \tag{25a}$$

$$R(z^{\text{M}} + z^{\text{s}}; \delta z^{\text{s}}) \;\; = 0 \quad \forall\, \delta z^{\text{s}} \in \mathbb{Z}^{\text{s}} \tag{25b}$$

Without introducing further assumptions (approximations), the dimension of the original problem has not changed, i.e. (25) represent two global problems whose solution requires the same computational effort as does (20). The trick is to use local approximations in the spirit of VMM, such that $z^{\text{s}} \approx \tilde{z}^{\text{s}}\{z^{\text{M}}\}$ are approximate solutions of the fine-scale equation (25b) for given z^{M}, i.e. $\tilde{z}^{\text{s}}$ represents the solution of RVE-problems for given boundary conditions

on z^{M}. Hence, for a given (implicit) functional relation $\tilde{z}^{\mathrm{s}}\{z^{\mathrm{M}}\}$, we may replace (25a) by the, approximate, homogenized problem

$$R(z^{\mathrm{M}} + \tilde{z}^{\mathrm{s}}\{z^{\mathrm{M}}\}; \delta z^{\mathrm{M}}) = 0 \quad \forall\, \delta z^{\mathrm{M}} \in \mathbb{Z}^{\mathrm{M},0} \tag{26}$$

which has the same dimension as (25a).

Referring to the actual problem of Stokes' flow, we can now expand (26) as follows

$$R^{\mathrm{v}}(\boldsymbol{v}^{\mathrm{M}} + \tilde{\boldsymbol{v}}^{\mathrm{s}}\{\boldsymbol{v}^{\mathrm{M}}, p^{\mathrm{M}}\}, p^{\mathrm{M}} + \tilde{p}^{\mathrm{s}}\{\boldsymbol{v}^{\mathrm{M}}, p^{\mathrm{M}}\}; \delta \boldsymbol{v}^{\mathrm{M}}) = 0 \quad \forall\, \delta \boldsymbol{v}^{\mathrm{M}} \in \mathbb{V}^{\mathrm{M},0} \tag{27a}$$

$$R^{\mathrm{p}}(\boldsymbol{v}^{\mathrm{M}} + \tilde{\boldsymbol{v}}^{\mathrm{s}}\{\boldsymbol{v}^{\mathrm{M}}, p^{\mathrm{M}}\}; \delta p^{\mathrm{M}}) = 0 \quad \forall\, \delta p^{\mathrm{M}} \in \mathbb{P}^{\mathrm{M}} \tag{27b}$$

However, in the present problem, it is only $\boldsymbol{v}$ that is partitioned into smooth and non-smooth fields, whereas we set $\tilde{p}^{\mathrm{s}} = p$. Hence, we have $z^{\mathrm{M}} = (\boldsymbol{v}^{\mathrm{M}}, 0)$ and $z^{\mathrm{s}} = (\boldsymbol{v}^{\mathrm{s}}, p)$, and (27a) is rewritten as

$$R^{\mathrm{v}}(\boldsymbol{v}^{\mathrm{M}} + \tilde{\boldsymbol{v}}^{\mathrm{s}}\{\boldsymbol{v}^{\mathrm{M}}\}, p\{\boldsymbol{v}^{\mathrm{M}}\}; \delta \boldsymbol{v}^{\mathrm{M}}) = 0 \quad \forall\, \delta \boldsymbol{v}^{\mathrm{M}} \in \mathbb{V}^{\mathrm{M},0} \tag{28}$$

whereas (27b) becomes irrelevant.

Remark: As a direct consequence of the assumption that is it only $\boldsymbol{v}$ that is partitioned in smooth and non-smooth fields, it is only the momentum balance that is relevant for the macroscale. The RVE problem thus means solving for $\tilde{\boldsymbol{v}}^{\mathrm{s}}\{\boldsymbol{v}^{\mathrm{M}}\}$ and $p\{\boldsymbol{v}^{\mathrm{M}}\}$ for given macroscale prolongation of the macroscopic velocity field $\boldsymbol{v}^{\mathrm{M}}$. □

Replacing the integrals in (28) by the volume averages, we directly obtain

$$R^{\mathrm{v}}(\boldsymbol{v}, p; \delta \boldsymbol{v}^{\mathrm{M}}) = -\bar{a}(\boldsymbol{v}, p; \delta \boldsymbol{v}^{\mathrm{M}}) = 0 \quad \forall\, \delta \boldsymbol{v}^{\mathrm{M}} \in \mathbb{V}^{\mathrm{M},0} \tag{29}$$

with $\boldsymbol{v} = \boldsymbol{v}^{\mathrm{M}} + \boldsymbol{v}^{\mathrm{s}}\{\boldsymbol{v}^{\mathrm{M}}\}$, $p = p\{\boldsymbol{v}^{\mathrm{M}}\}$. Here we introduced the homogenized variational form

$$\bar{a}(\boldsymbol{v}, p; \delta \boldsymbol{v}) \overset{\mathrm{def}}{=} \int_{\Omega} \left[a_{\square}(\boldsymbol{v}; \delta \boldsymbol{v}) + b_{\square}(p, \delta \boldsymbol{v}) - l_{\square}(\delta \boldsymbol{v}) \right] \mathrm{d}v \tag{30}$$

in terms of the RVE-forms

$$a_{\square}(\boldsymbol{v}; \delta \boldsymbol{v}) \overset{\mathrm{def}}{=} \langle \boldsymbol{\sigma}_{\mathrm{dev}}(\boldsymbol{d}) : [\delta \boldsymbol{v} \otimes \boldsymbol{\nabla}] \rangle_{\square} = \frac{1}{|\Omega_{\square}|} \int_{\Omega_{\square}^{\mathrm{part}}} \boldsymbol{\sigma}_{\mathrm{dev}}(\boldsymbol{d}) : [\delta \boldsymbol{v} \otimes \boldsymbol{\nabla}] \, \mathrm{d}v \tag{31a}$$

$$b_{\square}(p, \delta \boldsymbol{v}) \overset{\mathrm{def}}{=} -\langle [\delta \boldsymbol{v} \cdot \boldsymbol{\nabla}] p \rangle_{\square} = -\frac{1}{|\Omega_{\square}|} \int_{\Omega_{\square}^{\mathrm{part}}} [\delta \boldsymbol{v} \cdot \boldsymbol{\nabla}] p \, \mathrm{d}v \tag{31b}$$

$$l_{\square}(\delta \boldsymbol{v}) \overset{\mathrm{def}}{=} -\frac{1}{|\Omega_{\square}|} \int_{\Gamma_{\square}^{\mathrm{pore}}} \hat{\boldsymbol{\sigma}} : \left[\delta \boldsymbol{v} \otimes \hat{\boldsymbol{\nabla}} \right] \mathrm{d}a = -\frac{1}{|\Omega_{\square}|} \int_{\Gamma_{\square}^{\mathrm{pore}}} \gamma_{\mathrm{s}} \left[\delta \boldsymbol{v} \cdot \hat{\boldsymbol{\nabla}} \right] \mathrm{d}a \tag{31c}$$

where we introduced the volume average associated with particles inside the RVE-domain as

$$\langle [\bullet] \rangle_{\square} \overset{\mathrm{def}}{=} \frac{1}{|\Omega_{\square}|} \int_{\Omega_{\square}^{\mathrm{part}}} [\bullet] \, \mathrm{d}v. \tag{32}$$

In the present study, we only consider surface energy on the pore boundary, Γ^{pore}, which will be dominant, so for brevity, Γ^{cont} was dropped from (31c).

4.2 Generalized Macrohomogeneity Condition

Let us no return to the homogenized problem (26) and assume that there exists a potential $E(z)$ such that (26) represents the stationary point of $E(z)$, i.e. it is assumed that

$$R(z; \delta z) = E'_z(z; \delta z) = 0 \quad \forall\, \delta z \in \mathbb{Z}^0 \tag{33}$$

If we now introduce the approximation (restriction) $z \approx z^{\mathrm{M}} + \tilde{z}^{\mathrm{s}}\{z^{\mathrm{M}}\}$, equation (33) is equivalent to the condition

$$R(z^{\mathrm{M}} + \tilde{z}^{\mathrm{s}}\{z^{\mathrm{M}}\}; \delta z^{\mathrm{M}} + (\tilde{z}^{\mathrm{s}})'\{z^{\mathrm{M}}; \delta z^{\mathrm{M}}\}) = 0 \quad \forall\, \delta z^{\mathrm{M}} \in \mathbb{Z}^{\mathrm{M},0} \tag{34}$$

where $(\tilde{z}^{\mathrm{s}})'\{z^{\mathrm{M}};\delta z^{\mathrm{M}}\}$ denotes the sensitivity (or directional derivative) of $\tilde{z}^{\mathrm{s}}$ for a variation δz^{M} of the macroscale solution z^{M}. Hence, the choice of test function in (34) is restricted as compared to (33), and this restriction represents a Generalized Galerkin property in terms of the of the underlying macroscale functions in $\mathbb{Z}^{\mathrm{M}}$.

Now, we note that (34) is completely equivalent to the homogenized problem (26) if it is possible to satisfy the constraint

$$R(z^{\mathrm{M}}+\tilde{z}^{\mathrm{s}}\{z^{\mathrm{M}}\};(\tilde{z}^{\mathrm{s}})'\{z^{\mathrm{M}};\delta z^{\mathrm{M}}\})=0 \quad \forall\, \delta z^{\mathrm{M}}\in\mathbb{Z}^{\mathrm{M},0} \tag{35}$$

We thus refer to (35) as our generalized macro-homogeneity condition. If the condition is satisfied the VMM approximation in (34) is equivalent to the Galerkin (or energy type) formulation in (34). In the present case, we may expand (35) as

$$R^{\mathrm{v}}(\boldsymbol{v},p;(\tilde{\boldsymbol{v}}^{\mathrm{s}})'\{\boldsymbol{v}^{\mathrm{M}};\delta\boldsymbol{v}^{\mathrm{M}}\})+R^{\mathrm{p}}(\boldsymbol{v};p'\{\boldsymbol{v}^{\mathrm{M}};\delta\boldsymbol{v}^{\mathrm{M}}\})=0 \quad \forall\, \delta\boldsymbol{v}^{\mathrm{M}}\in\mathbb{V}^{\mathrm{M},0} \tag{36}$$

However, the last term in (36) is always zero since (21b) is always satisfied and $p'\{\bullet;\bullet\}\in\mathbb{P}$; hence, the condition reduces to

$$R^{\mathrm{v}}(\boldsymbol{v},p;(\tilde{\boldsymbol{v}}^{\mathrm{s}})'\{\boldsymbol{v}^{\mathrm{M}};\delta\boldsymbol{v}^{\mathrm{M}}\})=0 \quad \forall\, \delta\boldsymbol{v}^{\mathrm{M}}\in\mathbb{V}^{\mathrm{M},0} \tag{37}$$

where we recall that $\boldsymbol{v}=\boldsymbol{v}^{\mathrm{M}}+\bar{\boldsymbol{v}}^{\mathrm{s}}\{\boldsymbol{v}^{\mathrm{M}}\}$, $p=p\{\boldsymbol{v}^{\mathrm{M}}\}$.

Finally we note that (37) can be rewritten in terms of the contributions of residuals defined on each RVE as

$$R^{\mathrm{v}}(\boldsymbol{v},p;(\tilde{\boldsymbol{v}}^{\mathrm{s}})'\{\boldsymbol{v}^{\mathrm{M}};\delta\boldsymbol{v}^{\mathrm{M}}\})=\int_{\Omega}R^{\mathrm{v}}_{\square}(\boldsymbol{v},p,(\tilde{\boldsymbol{v}}^{\mathrm{s}})'\{\boldsymbol{v}^{\mathrm{M}};\delta\boldsymbol{v}^{\mathrm{M}}\})(\bar{\boldsymbol{x}})\,\mathrm{d}v \tag{38}$$

where $R^{\mathrm{v}}_{\square}$ is the RVE-residual that is given as

$$R^{\mathrm{v}}_{\square}(\boldsymbol{v},p;\delta\boldsymbol{v}^{\mathrm{s}})\overset{\mathrm{def}}{=}l_{\square}(\delta\boldsymbol{v}^{\mathrm{s}})-a_{\square}(\boldsymbol{v};\delta\boldsymbol{v}^{\mathrm{s}})-b_{\square}(p,\delta\boldsymbol{v}^{\mathrm{s}})=-\frac{1}{|\Omega_{\square}|}\int_{\Gamma_{\square}}\boldsymbol{t}\cdot\delta\boldsymbol{v}^{\mathrm{s}}\,\mathrm{d}a \tag{39}$$

where $\boldsymbol{t}\overset{\mathrm{def}}{=}\boldsymbol{\sigma}\cdot\boldsymbol{n}$ is the (unknown) traction.

Obviously, a sufficient condition for (37) to hold true is to require the RVE-residual to vanish on each RVE, i.e. to ensure that

$$R^{\mathrm{v}}_{\square}(\boldsymbol{v},p;(\tilde{\boldsymbol{v}}^{\mathrm{s}})'\{\boldsymbol{v}^{\mathrm{M}};\delta\boldsymbol{v}^{\mathrm{M}}\})=0 \quad \forall\, \delta\boldsymbol{v}^{\mathrm{M}}\in\mathbb{V}^{\mathrm{M},0}|_{\Omega_{\square}} \tag{40}$$

An even stronger condition is to require that $R^{\mathrm{v}}_{\square}(\boldsymbol{v},p;\delta\boldsymbol{v}^{\mathrm{s}})=0$ for any given $\delta\boldsymbol{v}^{\mathrm{s}}$ in a given set of functions that is defined locally for the considered RVE without requiring any implicit (or explicit) coupling to the sensitivity field $(\tilde{\boldsymbol{v}}^{\mathrm{s}})'\{\boldsymbol{v}^{\mathrm{M}};\delta\boldsymbol{v}^{\mathrm{M}}\}$, which defines a restricted choice of test functions. In such a case it can be shown that the condition is precisely the classical Hill-Mandel macrohomogeneity condition.

4.3 Macroscale Problem for First Order Homogenization

In standard fashion the macroscale velocity field $\bar{\boldsymbol{v}}$ is prolonged to the RVE, whereby the explicit part, which is denoted $\boldsymbol{v}^{\mathrm{M}}$, is assumed to vary only *linearly* (derivatives up to first order are included) within the RVE, i.e.

$$\boldsymbol{v}^{\mathrm{M}}(\bar{\boldsymbol{x}};\boldsymbol{x})=\bar{\boldsymbol{d}}(\bar{\boldsymbol{x}})\cdot[\boldsymbol{x}-\bar{\boldsymbol{x}}] \text{ for } \boldsymbol{x}\in\Omega_{\square} \tag{41}$$

Obviously, the link between $\bar{\boldsymbol{v}}$ and $\boldsymbol{v}^{\mathrm{M}}$ is given via the macroscale rate-of-deformation tensor $\bar{\boldsymbol{d}}$, defined as

$$\bar{\boldsymbol{d}}(\bar{\boldsymbol{x}})\overset{\mathrm{def}}{=}[\bar{\boldsymbol{v}}\otimes\boldsymbol{\nabla}]^{\mathrm{sym}}|_{\bar{\boldsymbol{x}}}. \tag{42}$$

The expression in (41) may conveniently be rewritten as

$$\boldsymbol{v}^{\mathrm{M}}=\bar{\boldsymbol{d}}\cdot[\boldsymbol{x}-\bar{\boldsymbol{x}}]=\sum_{i,j=1}^{n_{\mathrm{dim}}}\hat{\boldsymbol{v}}^{\mathrm{M}(ij)}\bar{d}_{ij} \tag{43}$$

in terms of the unit velocity fields $\hat{\boldsymbol{v}}^{\mathrm{M}(ij)}$ that are given as

$$\hat{\boldsymbol{v}}^{\mathrm{M}(ij)}\overset{\mathrm{def}}{=}\boldsymbol{e}_i\otimes\boldsymbol{e}_j\cdot[\boldsymbol{x}-\bar{\boldsymbol{x}}]=\boldsymbol{e}_i\,[x_j-\bar{x}_j]\,. \tag{44}$$

The corresponding unit rate-of-deformation fields are given as

$$\hat{\boldsymbol{d}}^{\mathrm{M}(ij)} \stackrel{\mathrm{def}}{=} [\hat{\boldsymbol{v}}^{\mathrm{M}(ij)} \otimes \boldsymbol{\nabla}]^{\mathrm{sym}} = [\boldsymbol{e}_i \otimes \boldsymbol{e}_j]^{\mathrm{sym}}\,. \tag{45}$$

From (30) and (43) we now obtain that $\bar{a}(\boldsymbol{v}, p; \delta\boldsymbol{v}^{\mathrm{M}})$ can be expressed as

$$\bar{a}(\boldsymbol{v}, p; \delta\boldsymbol{v}^{\mathrm{M}}) = \int_\Omega \sum_{i,j=1}^{n_{\mathrm{dim}}} \Big[a_\square(\boldsymbol{v}; \hat{\boldsymbol{v}}^{\mathrm{M}(ij)}) + b_\square(p, \hat{\boldsymbol{v}}^{\mathrm{M}(ij)}) - l_\square(\hat{\boldsymbol{v}}^{\mathrm{M}(ij)})\Big]\, \delta\bar{d}_{ij}\, \mathrm{d}v. \tag{46}$$

Upon noting the definitions in (31), we obtain the macroscale internal virtual work (space-variational) formulation

$$\bar{a}(\boldsymbol{v}, p; \delta\boldsymbol{v}^{\mathrm{M}}) = \bar{a}\{\bar{\boldsymbol{v}}; \delta\bar{\boldsymbol{v}}\} \stackrel{\mathrm{def}}{=} \int_\Omega \bar{\boldsymbol{\sigma}}\{\bar{\boldsymbol{d}}\} : [\delta\bar{\boldsymbol{v}} \otimes \boldsymbol{\nabla}]\, \mathrm{d}v \tag{47}$$

where the energy-conjugated macroscale stress tensor $\bar{\boldsymbol{\sigma}}$ is deduced from comparing (46) and (47) as

$$\begin{aligned}
\bar{\boldsymbol{\sigma}} &= \langle\boldsymbol{\sigma}\rangle_\square - \sum_{i,j=1}^{n_{\mathrm{dim}}} l_\square(\hat{\boldsymbol{v}}^{\mathrm{M}(ij)})\boldsymbol{e}_i \otimes \boldsymbol{e}_j \\
&= \frac{1}{|\Omega_\square|}\int_{\partial\Omega_\square^{\mathrm{part}}} [\boldsymbol{t} \otimes [\boldsymbol{x} - \bar{\boldsymbol{x}}]]^{\mathrm{sym}}\, \mathrm{d}a - \frac{1}{|\Omega_\square|}\int_{\Gamma_\square^{\mathrm{pore}}} [\boldsymbol{t}_{\mathrm{s}} \otimes [\boldsymbol{x} - \bar{\boldsymbol{x}}]]^{\mathrm{sym}}\, \mathrm{d}a \\
&= \frac{1}{|\Omega_\square|}\int_{\Gamma_\square} [\boldsymbol{t} \otimes [\boldsymbol{x} - \bar{\boldsymbol{x}}]]^{\mathrm{sym}}\, \mathrm{d}a
\end{aligned} \tag{48}$$

where it was used that $\boldsymbol{t} = \boldsymbol{t}_{\mathrm{s}}$ on $\Gamma_\square^{\mathrm{pore}}$ and $\partial\Omega_\square^{\mathrm{part}} = \Gamma_\square \cup \Gamma_\square^{\mathrm{pore}}$.

Hence, the macroscale problem can be written as the residual equation

$$\bar{R}\{\bar{\boldsymbol{v}}; \delta\bar{\boldsymbol{v}}\} \stackrel{\mathrm{def}}{=} -\bar{a}\{\bar{\boldsymbol{v}}; \delta\bar{\boldsymbol{v}}\} = 0, \quad \forall\delta\bar{\boldsymbol{v}} \in \bar{\mathbb{V}}^0 \tag{49}$$

where $\bar{\mathbb{V}}^0$ is the test space such that each $\bar{\boldsymbol{v}} \in \bar{\mathbb{V}}^0$ vanishes on the Dirichlet part of the macroscale domain.

Remark: As to the proper relation between $\bar{\boldsymbol{d}}$ and the local field $\boldsymbol{d}$, we note that

$$\bar{\boldsymbol{d}} = \langle\boldsymbol{d}\rangle_\square - \frac{1}{|\Omega_\square|}\int_{\Gamma_\square^{\mathrm{pore}}} [\boldsymbol{v} \otimes \boldsymbol{n}]^{\mathrm{sym}}\, \mathrm{d}a = \frac{1}{|\Omega_\square|}\int_{\Gamma_\square} [\boldsymbol{v} \otimes \boldsymbol{n}]^{\mathrm{sym}}\, \mathrm{d}a. \tag{50}$$

□

In order to solve (49) by Newton iterations, we need the tangent form

$$\bar{a}'\{\bar{\boldsymbol{v}}; \delta\bar{\boldsymbol{v}}, \Delta\bar{\boldsymbol{v}}\} \stackrel{\mathrm{def}}{=} \int_\Omega [\delta\bar{\boldsymbol{v}} \otimes \boldsymbol{\nabla}] : \bar{\mathbf{E}}_{\mathrm{T}} : [\Delta\bar{\boldsymbol{v}} \otimes \boldsymbol{\nabla}]\, \mathrm{d}v. \tag{51}$$

The appropriate macroscale algorithmic tangent stiffness tensor, $\bar{\mathbf{E}}_{\mathrm{T}}$, is obtained upon linearizing the relation $\bar{\boldsymbol{\sigma}}\{\bar{\boldsymbol{d}}\}$ as follows

$$\mathrm{d}\bar{\boldsymbol{\sigma}}\{\bar{\boldsymbol{d}}\} = \bar{\mathbf{E}}_{\mathrm{T}}\{\bar{\boldsymbol{d}}\} : \mathrm{d}\bar{\boldsymbol{d}} \tag{52}$$

and it is computed by *linearization* of the RVE-problem, which leads to a *sensitivity* or *tangent* problem. How to formulate and solve this sensitivity problem in practice depends strongly on the actual choice of prolongation condition (as will be discussed below). In particular, the specific variational setting for every type of prolongation condition is different.

5 RVE-Problem for Given Macroscale Velocity Gradient

5.1 Variational Format – Dirichlet Boundary Conditions

The task is to obtain the homogenized response for a prescribed value of the macroscale rate-of-deformation $\bar{\boldsymbol{d}}$ and to return the resulting macroscopic stress $\bar{\boldsymbol{\sigma}}$ after homogenization to the macroscale problem (49), whereby

expressions for $\bar{\boldsymbol{\sigma}}$ in (48) and $\bar{\boldsymbol{d}}$ in (50) are noted. Equation (50) for prescribed value of $\bar{\boldsymbol{d}}$ is trivially satisfied if Dirichlet boundary conditions on the local velocity field is imposed on the external boundary as follows (in complete analogy with solid modeling, e.g. elasticity, in the Lagrangian description)

$$\boldsymbol{v} = \boldsymbol{v}^{\mathrm{M}} = \bar{\boldsymbol{d}} \cdot [\boldsymbol{x} - \bar{\boldsymbol{x}}] \text{ on } \Gamma_{\square}. \tag{53}$$

Prescribing the velocity on all external boundaries requires the existence of internal pores; hence, such a boundary condition will no longer by applicable when the porosity vanishes.

We are then lead to defining the following trial and test spaces

$$\mathbb{V}^0_{\square} = \{\boldsymbol{v} \text{ sufficiently regular in } \Omega_{\square},\ \boldsymbol{v} = \boldsymbol{0} \text{ on } \Gamma_{\square}\} \tag{54}$$
$$\mathbb{P}_{\square} = \{p \in L_2(\Omega_{\square})\} \tag{55}$$

The appropriate space-variational format of the RVE-problem can now be formulated as follows: Find $\boldsymbol{v}^{\mathrm{s}} \in \mathbb{V}^0_{\square}$, and $p \in \mathbb{P}_{\square}$ that, for given value of the macroscale $\bar{\boldsymbol{d}}$, solve the system

$$a_{\square}(\boldsymbol{v}^{\mathrm{M}}(\bar{\boldsymbol{d}}) + \boldsymbol{v}^{\mathrm{s}}; \delta\boldsymbol{v}^{\mathrm{s}}) + b_{\square}(p, \delta\boldsymbol{v}^{\mathrm{s}}) = l_{\square}(\delta\boldsymbol{v}^{\mathrm{s}}) \quad \forall \delta\boldsymbol{v}^{\mathrm{s}} \in \mathbb{V}^0_{\square} \tag{56a}$$
$$b_{\square}(\delta p, \boldsymbol{v}^{\mathrm{M}}(\bar{\boldsymbol{d}}) + \boldsymbol{v}^{\mathrm{s}}) = 0 \quad \forall \delta p \in \mathbb{P}_{\square}, \tag{56b}$$

where we made explicit use of the local decomposition (within a given RVE) $\boldsymbol{v}\{\bar{\boldsymbol{d}}\} = \boldsymbol{v}^{\mathrm{M}}(\bar{\boldsymbol{d}}) + \boldsymbol{v}^{\mathrm{s}}\{\bar{\boldsymbol{d}}\}$ in terms of the macroscale part, $\boldsymbol{v}^{\mathrm{M}}(\bar{\boldsymbol{d}}) = \bar{\boldsymbol{d}} \cdot [\boldsymbol{x} - \bar{\boldsymbol{x}}]$ and the fluctuation part, $\boldsymbol{v}^{\mathrm{s}}\{\bar{\boldsymbol{d}}\}$.

The RVE-problem (56) must be solved iteratively in practice due to the subscale nonlinearities. To this end, we first rewrite (56) as the residual relations

$$R^{\mathrm{v}}_{\square}(\boldsymbol{v}^{\mathrm{s}}, p; \delta\boldsymbol{v}^{\mathrm{s}}) \stackrel{\mathrm{def}}{=} l_{\square}(\delta\boldsymbol{v}^{\mathrm{s}}) - a_{\square}(\boldsymbol{v}^{\mathrm{M}}(\bar{\boldsymbol{d}}) + \boldsymbol{v}^{\mathrm{s}}; \delta\boldsymbol{v}^{\mathrm{s}}) - b_{\square}(p, \delta\boldsymbol{v}^{\mathrm{s}}) = 0 \quad \forall \delta\boldsymbol{v}^{\mathrm{s}} \in \mathbb{V}^0_{\square} \tag{57}$$
$$R^{\mathrm{p}}_{\square}(\boldsymbol{v}^{\mathrm{s}}; \delta p) \stackrel{\mathrm{def}}{=} -b_{\square}(\delta p, \boldsymbol{v}^{\mathrm{M}}(\bar{\boldsymbol{d}}) + \boldsymbol{v}^{\mathrm{s}}) = 0 \quad \forall \delta p \in \mathbb{P}_{\square} \tag{58}$$

Newton's iteration method for finding the unknown $\boldsymbol{v}^{\mathrm{s}}$ and p for given $\bar{\boldsymbol{d}}$ then becomes: For $k = 1, 2, \ldots$, compute

$$\boldsymbol{v}^{\mathrm{s}(k+1)} = \boldsymbol{v}^{\mathrm{s}(k)} + \Delta\boldsymbol{v}^{\mathrm{s}}, \quad p^{(k+1)} = p^{(k)} + \Delta p \tag{59}$$

where the iterative updates $\Delta\boldsymbol{v}^{\mathrm{s}} \in \mathbb{V}^0_{\square}$ and $\Delta p \in \mathbb{P}_{\square}$ are solved from the tangent equations

$$(a_{\square})'(\bullet^{(k)}; \delta\boldsymbol{v}^{\mathrm{s}}, \Delta\boldsymbol{v}^{\mathrm{s}}) + b_{\square}(\Delta p, \delta\boldsymbol{v}^{\mathrm{s}}) = R^{\mathrm{v}}_{\square}(\bullet^{(k)}; \delta\boldsymbol{v}^{\mathrm{s}}) \quad \forall \delta\boldsymbol{v}^{\mathrm{s}} \in \mathbb{V}^0_{\square}, \tag{60a}$$
$$b_{\square}(\delta p, \Delta\boldsymbol{v}^{\mathrm{s}}) = R^{\mathrm{p}}_{\square}(\bullet^{(k)}; \delta p) \quad \forall \delta p \in \mathbb{P}_{\square}. \tag{60b}$$

until the residuals are sufficiently small. The tangent form $(a_{\square})'$ is given explicitly as

$$(a_{\square})'(\bullet; \delta\boldsymbol{v}^{\mathrm{s}}, \Delta\boldsymbol{v}^{\mathrm{s}}) = \langle [\delta\boldsymbol{v} \otimes \boldsymbol{\nabla}] : \mathsf{E}_{\mathrm{T,dev}}(\bullet) : [\Delta\boldsymbol{v}^{\mathrm{s}} \otimes \boldsymbol{\nabla}] \rangle_{\square}. \tag{61}$$

5.2 Macroscale ATS-Tensor – Dirichlet Boundary Conditions

The macroscale ATS-tensor, denoted $\bar{\mathsf{E}}_{\mathrm{T}}$ and defined in (52), is obtained for perturbations of the RVE-solution expressed in terms of perturbations of $\bar{\boldsymbol{d}}$. Firstly, it is clear that this tensor is needed for the macroscale iterations based on Newton's method. However, it is important to note that $\bar{\mathsf{E}}_{\mathrm{T}}$ is required also for other purposes. One example is goal-oriented discretization error computation utilizing a dual problem that is based on $\bar{\mathsf{E}}_{\mathrm{T}}$, cf. Larsson and Runesson (2006) (not further considered in this paper).

It turns out to be convenient to compute unit fluctuation fields or, rather, *sensitivity fields*, corresponding to a unit variation of the macroscale variable $\bar{\boldsymbol{d}}$. Hence, we shall need to compute the differentials

$$\mathrm{d}\boldsymbol{v} = \mathrm{d}\boldsymbol{v}^{\mathrm{M}} + \mathrm{d}\boldsymbol{v}^{\mathrm{s}} = \mathrm{d}\boldsymbol{v}^{\mathrm{M}} + (\boldsymbol{v}^{\mathrm{s}})'\{\boldsymbol{v}^{\mathrm{M}}; \mathrm{d}\boldsymbol{v}^{\mathrm{M}}\} \tag{62a}$$
$$\mathrm{d}p = (p)'\{\boldsymbol{v}^{\mathrm{M}}; \mathrm{d}\boldsymbol{v}^{\mathrm{M}}\} \tag{62b}$$

in terms of $\mathrm{d}\bar{\boldsymbol{d}}$, whereby $(\boldsymbol{v}^{\mathrm{s}})'$ and $(p)'$ denote directional derivatives and it is emphasized that $\boldsymbol{v}^{\mathrm{s}}\{\boldsymbol{v}^{\mathrm{M}}\}$ and $p\{\boldsymbol{v}^{\mathrm{M}}\}$ are implicit relations.

Upon using the identity $\mathrm{d}\bar{\boldsymbol{\sigma}} = \langle \mathrm{d}\boldsymbol{\sigma} \rangle_\square$ such that

$$\mathrm{d}\bar{\sigma}_{ij} = \langle \mathrm{d}\boldsymbol{\sigma} : [\boldsymbol{e}_i \otimes \boldsymbol{e}_j]^{\mathrm{sym}} \rangle_\square = \langle \mathrm{d}\boldsymbol{\sigma} : \hat{\boldsymbol{d}}^{\mathrm{M}(ij)} \rangle_\square = \mathrm{d}\Big[\langle \boldsymbol{\sigma} : \hat{\boldsymbol{d}}^{\mathrm{M}(ij)} \rangle_\square \Big] \tag{63}$$

together with the relation

$$\langle \boldsymbol{\sigma} : \delta \boldsymbol{d} \rangle_\square = a_\square(\boldsymbol{v}; \delta \boldsymbol{v}) + b_\square(p; \delta \boldsymbol{v}) \tag{64}$$

we may choose $\delta \boldsymbol{d} = \hat{\boldsymbol{d}}^{\mathrm{M}(ij)}$ in (64) to obtain the representation of $\mathrm{d}\bar{\sigma}_{ij}$ as follows

$$\begin{aligned} \mathrm{d}\bar{\sigma}_{ij} &= \mathrm{d}\Big[\langle \boldsymbol{\sigma} : \hat{\boldsymbol{d}}^{\mathrm{M}(ij)} \rangle_\square \Big] = \mathrm{d}\Big[a_\square(\boldsymbol{v}; \hat{\boldsymbol{v}}^{\mathrm{M}(ij)}) + b_\square(p; \hat{\boldsymbol{v}}^{\mathrm{M}(ij)}) \Big] \\ &= (a_\square)'(\boldsymbol{v}; \hat{\boldsymbol{v}}^{\mathrm{M}(ij)}, \mathrm{d}\boldsymbol{v}) + b_\square(\mathrm{d}p, \hat{\boldsymbol{v}}^{\mathrm{M}(ij)}) \end{aligned} \tag{65}$$

where it was used that $b_\square$ is a bilinear form.

Next, we conclude that the state equation (56) must hold for $\bar{\boldsymbol{d}}$ as well as for a perturbed state $\bar{\boldsymbol{d}} + \mathrm{d}\bar{\boldsymbol{d}}$. However, a given change $\mathrm{d}\bar{\boldsymbol{d}}$ gives rise to a change, not only in $\mathrm{d}\boldsymbol{v}^{\mathrm{M}}$, but also in $\mathrm{d}\boldsymbol{v}^{\mathrm{s}} \in \mathbb{V}^0_\square$ and $\mathrm{d}p \in \mathbb{P}_\square$. Upon linearizing (56), while using (62) we obtain the appropriate tangent problem:

$$(a_\square)'(\boldsymbol{v}^{\mathrm{M}}(\bar{\boldsymbol{d}}) + \boldsymbol{v}^{\mathrm{s}}; \delta \boldsymbol{v}^{\mathrm{s}}, \mathrm{d}\boldsymbol{v}^{\mathrm{M}} + \mathrm{d}\boldsymbol{v}^{\mathrm{s}}) + b_\square(\mathrm{d}p, \delta \boldsymbol{v}^{\mathrm{s}}) = 0 \quad \forall \delta \boldsymbol{v}^{\mathrm{s}} \in \mathbb{V}^0_\square \tag{66a}$$

$$b_\square(\delta p, \mathrm{d}\boldsymbol{v}^{\mathrm{M}} + \mathrm{d}\boldsymbol{v}^{\mathrm{s}}) = 0 \quad \forall \delta p \in \mathbb{P}_\square \tag{66b}$$

from which $\mathrm{d}\boldsymbol{v}^{\mathrm{s}}$ and $\mathrm{d}p$ can be solved for any given $\mathrm{d}\boldsymbol{v}^{\mathrm{M}} = \mathrm{d}\bar{\boldsymbol{d}} \cdot [\boldsymbol{x} - \bar{\boldsymbol{x}}]$.

In analogy with the definition of $\hat{\boldsymbol{v}}^{\mathrm{M}(ij)}$ in (43), we then introduce the unit fields, or sensitivities, $\hat{\boldsymbol{v}}^{\mathrm{s}(ij)}$ and $\hat{p}^{(ij)}$, due to a unit value of the components $\mathrm{d}\bar{d}_{ij}$, via the *ansatz*

$$\mathrm{d}\boldsymbol{v}^{\mathrm{s}} = \sum_{i,j} \hat{\boldsymbol{v}}^{\mathrm{s}(ij)} \, \mathrm{d}\bar{d}_{ij}, \quad \mathrm{d}p = \sum_{i,j} \hat{p}^{(ij)} \, \mathrm{d}\bar{d}_{ij} \tag{67}$$

which may be inserted into (66) to give the equations that must hold for $k, l = 1, 2, \ldots, n_{\mathrm{dim}}$

$$(a_\square)'(\bullet; \delta \boldsymbol{v}^{\mathrm{s}}, \hat{\boldsymbol{v}}^{\mathrm{s}(kl)}) + b_\square(\hat{p}^{(kl)}, \delta \boldsymbol{v}^{\mathrm{s}}) = -(a_\square)'(\bullet; \delta \boldsymbol{v}^{\mathrm{s}}, \hat{\boldsymbol{v}}^{\mathrm{M}(kl)}) \quad \forall \delta \boldsymbol{v}^{\mathrm{s}} \in \mathbb{V}^0_\square, \tag{68a}$$

$$b_\square(\delta p, \hat{\boldsymbol{v}}^{\mathrm{s}(kl)}) = -b_\square(\delta p, \hat{\boldsymbol{v}}^{\mathrm{M}(kl)}) \qquad \forall \delta p \in \mathbb{P}_\square. \tag{68b}$$

We may express the source terms in (68) more explicitly as

$$(a_\square)'(\bullet; \delta \boldsymbol{v}, \hat{\boldsymbol{v}}^{\mathrm{M}(kl)}) = \langle \delta \boldsymbol{d} : \mathbf{E}_{\mathrm{T,dev}} : \hat{\boldsymbol{d}}^{\mathrm{M}(kl)} \rangle_\square = \langle [\delta \boldsymbol{v} \otimes \boldsymbol{\nabla}]^{\mathrm{sym}} : (\mathbf{E}_{\mathrm{T,dev}})_{kl} \rangle_\square \tag{69a}$$

$$\begin{aligned} b_\square(\delta p, \hat{\boldsymbol{v}}^{\mathrm{M}(kl)}) &= -\langle \delta p \, \boldsymbol{I} : \hat{\boldsymbol{d}}^{\mathrm{M}(kl)} \rangle_\square = -\langle \delta p \rangle_\square \, \delta_{kl} \\ &= -\frac{1}{|\Omega_\square|} \int_{\Gamma_\square} \delta p \, n_k [x_l - \bar{x}_l] \, \mathrm{d}a \end{aligned} \tag{69b}$$

The unit fields $\hat{\boldsymbol{v}}^{\mathrm{s}(ij)}$ and $\hat{p}^{(ij)}$ are solved from (68) and inserted into (65) to give the explicit expression for $\bar{\mathbf{E}}_{\mathrm{T}}$

$$\bar{\mathbf{E}}_{\mathrm{T}} = \langle \mathbf{E}_{\mathrm{T,dev}} \rangle_\square + \sum_{k,l=1}^{n_{\mathrm{dim}}} \langle \mathbf{E}_{\mathrm{T,dev}} : \hat{\boldsymbol{d}}^{\mathrm{s}(kl)} \rangle_\square \otimes \boldsymbol{e}_k \otimes \boldsymbol{e}_l - \sum_{k,l=1}^{n_{\mathrm{dim}}} \boldsymbol{I} \otimes \langle \hat{p}^{(kl)} \rangle_\square \boldsymbol{e}_k \otimes \boldsymbol{e}_l \tag{70}$$

where we introduced the (obvious) notation $\hat{\boldsymbol{d}}^{\mathrm{s}(kl)} \overset{\mathrm{def}}{=} \Big[\hat{\boldsymbol{v}}^{\mathrm{s}(kl)} \otimes \boldsymbol{\nabla} \Big]^{\mathrm{sym}}$ and the following identities were used

$$(a_\square)'(\bullet; \hat{\boldsymbol{v}}^{\mathrm{M}(ij)}, \hat{\boldsymbol{v}}^{\mathrm{M}(kl)}) = \langle (\mathbf{E}_{\mathrm{T,dev}})_{ijkl} \rangle_\square, \tag{71}$$

$$(a_\square)'(\bullet; \hat{\boldsymbol{v}}^{\mathrm{M}(ij)}, \hat{\boldsymbol{v}}^{\mathrm{s}(kl)}) = \langle (\mathbf{E}_{\mathrm{T,dev}} : \hat{\boldsymbol{d}}^{\mathrm{s}(kl)})_{ij} \rangle_\square \tag{72}$$

$$b_\square(\hat{p}^{(kl)}, \hat{\boldsymbol{v}}^{\mathrm{M}(ij)}) = -\delta_{ij} \langle \hat{p}^{(kl)} \rangle_\square \tag{73}$$

6 Computational Strategy

6.1 Preliminaries

The main computational challenge in solving the RVE-problem is, in terms of FE-analysis, to (i) trace the actual material motion and (ii) update the FE-mesh. This challenge is due to the fact that very large deformations occur, accompanied by severe topology changes. In particular, it is necessary to trace the motion of the moving boundary $\Gamma_{\square}^{\mathrm{mov}}(t)$. For example, this is required in order to trace changes of the macroscale porosity (relative density) during the sintering process. In this case, we track all boundaries in each RVE, i.e. $\Gamma_{\square}^{\mathrm{mov}} = \Gamma_{\square}^{\mathrm{pore}} \cup \Gamma_{\square}^{\mathrm{cont}} \cup \Gamma_{\square}$.

To be more specific, we thus set out from the state given at the time t_{n-1} in terms of a given configuration, in particular given moving surface ${}^{n-1}\Gamma_{\square}^{\mathrm{mov}} \stackrel{\mathrm{def}}{=} \Gamma_{\square}^{\mathrm{mov}}(t_{n-1})$, and the associated mesh ${}^{n-1}\mathcal{M}_{\square}$. We seek the state at the updated time $t_n = t_{n-1} + \Delta t$, whereby the time interval $I_n = (t_{n-1}, t_n)$ is taken as the appropriate one from time discretization. This means to obtain the updated configuration of the moving boundary, ${}^{n}\Gamma_{\square}^{\mathrm{mov}} \stackrel{\mathrm{def}}{=} \Gamma_{\square}^{\mathrm{mov}}(t_n)$, along with the mesh ${}^{n}\mathcal{M}_{\square}$.

A large number of strategies for handling large deformations have been proposed in the literature since the 1990's; a comprehensive review is given by Dettmer and Perić (2006), and references therein.

6.2 Review of Surface Tracking Methods

The task is to compute the positions of the boundary placement ${}^{n}\boldsymbol{x} = \boldsymbol{x}(\boldsymbol{X}, t_n) \in {}^{n}\Gamma_{\square}^{\mathrm{mov}}$ knowing the placement ${}^{n-1}\boldsymbol{x} = \boldsymbol{x}(\boldsymbol{X}, t_{n-1}) \in {}^{n-1}\Gamma_{\square}^{\mathrm{mov}}$. For simplicity of notation, but without jeopardizing generality, we choose here to consider the reference position of the material point in question to be identical to the last known position, i.e. we set $\boldsymbol{X} = {}^{n-1}\boldsymbol{x}$. The basic update formula is then

$$ {}^{n}\boldsymbol{x} = {}^{n-1}\boldsymbol{x} + \tilde{\boldsymbol{v}}\Delta t \tag{74} $$

where $\tilde{\boldsymbol{v}}$ is a suitably chosen representation for the material velocity. The two basic choices of $\tilde{\boldsymbol{v}}$ are

$$ \tilde{\boldsymbol{v}} = \begin{cases} {}^{n-1}\boldsymbol{v} = \boldsymbol{v}(\boldsymbol{X}, t_{n-1}) & \text{Forward Euler, IE,} \\ {}^{n}\boldsymbol{v} = \boldsymbol{v}(\boldsymbol{X}, t_n) & \text{Backward Euler, TUL} \end{cases} \tag{75} $$

The choice $\tilde{\boldsymbol{v}} = {}^{n-1}\boldsymbol{v}$ is the simplest (and most straightforward) one, and it corresponds to an Incremental Eulerian (IE) description of the motion. This means that the velocity field is computed for the *known* configuration ${}^{n-1}\Omega_{\square} \stackrel{\mathrm{def}}{=} \Omega_{\square}(t_{n-1})$. As a consequence, a sequence of creeping flow RVE-problems are solved for consecutively updated boundaries.

The choice $\tilde{\boldsymbol{v}} = {}^{n}\boldsymbol{v}$, on the other hand, corresponds to a Truly Updated Lagrangian (TUL) description of the motion. (The notion TUL was introduced in order to avoid confusion with the UL description that is defined by choosing ${}^{n-1}\Omega \stackrel{\mathrm{def}}{=} \Omega(t_{n-1})$ as the reference configuration and computational domain). A characteristic feature is that the velocity field is computed for the *a priori unknown* configuration ${}^{n}\Omega_{\square} \stackrel{\mathrm{def}}{=} \Omega_{\square}(t_n)$, which is taken as the reference configuration for stress computation as well as serving as the computational domain for the space-variational formulation of the RVE-problem. As a consequence, the computational domain is not known beforehand (since it is rather part of the solution), but it suffices to use the Cauchy stress that is obtained directly from the constitutive model in the case that a flow model is used.

Remark: In the conventional Updated Lagrangian description (UL), the computational domain is *fixed* in the considered time interval I_n, but the appropriate 1st PK stress is needed in the equilibrium equation and must be obtained by a pullback from ${}^{n}\Omega$ to ${}^{n-1}\Omega$. □

The choice of description of motion is basically a matter of taste and ease of computation; however, we shall adopt the IE since it is more natural in conjunction with a flow model. In fact, in the absence of acceleration, the formal similarity between TUL and the IE description is striking. The difference is only present in the treatment of the motion of the free boundary, which is fixed in the IE description while it is part of the solution in the TUL.

6.3 Updating the Subscale FE-Mesh

6.3.1 Topology Description

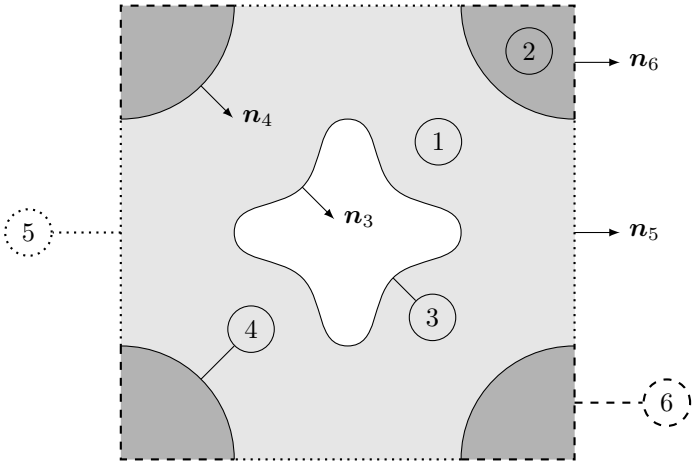

Figure 5: Possible boundaries and regions required by the topology description

Once a velocity $\tilde{\boldsymbol{v}}$ has been obtained from the FE analysis the topology description must be updated. If topological changes like merging and vanishing pores do occur, or if the FE-mesh is too deformed, a new mesh ${}^{n}\mathcal{M}_{\square}$ must be constructed from the updated topology description. This means that the topology description must contain all necessary information for reconstructing the entire problem with regard to all boundaries and bulk regions, as illustrated in Figure 5. Bulk regions outside and inside a given boundary are defined by normals in the positive and negative direction, respectively. For the example in Figure 5, the bulk regions are determined by $\{-,-,0,1,0,0\}^{+}$ and $\{-,-,1,2,1,2\}^{-}$. With this state information, it is a simple procedure to define consistent tables on how the boundaries behave in contact, e.g. when boundary regions with the same number come in contact and the boundary vanishes. From a raw mesh, typically a convex hull generated by the well known Delaunay meshing program Triangle (cf. Shewchuk (1996)), every bulk element can easily obtain its respective region number from the boundaries, and zero region number would indicate a hole in the mesh. This step also allows for the possibility to check the consistency of the mesh. If a bulk element is not assigned to any region or multiple different region, the topology description is broken. In order to construct the regions from edge segments, some modifications to the default procedure used in Triangle was necessary.

When each region in a new mesh has been numbered all that is left is to apply the corresponding material and (if any) boundary conditions. If any state variables are used, they can also be mapped for each region. This setup for tracking boundary and bulk regions offers a straightforward procedure on creating a complete FE problem. It also extends to 3D without any modification, and can handle arbitrary number of regions, with the possibility to check the internal consistency.

6.3.2 Grid-Based Particle Method

To store the topology state in Figure 5 a grid-based particle method (GBPM) has been implemented. The implementation is based on the description described in Leung and Zhao (2009a,b). The method is extended for generating a Planar Straight Line Graph (PSLG) necessary for meshing with the software Triangle;

1. Enumerate all foot points. Very close points attain the same number.
2. Find the neighboring particles. Reject particles according to the same conditions as for the local reconstruction.
3. Find the two closest neighbors in the positive and negative direction for all nodes. Append these two new segments.
4. Clear out duplicated segments.

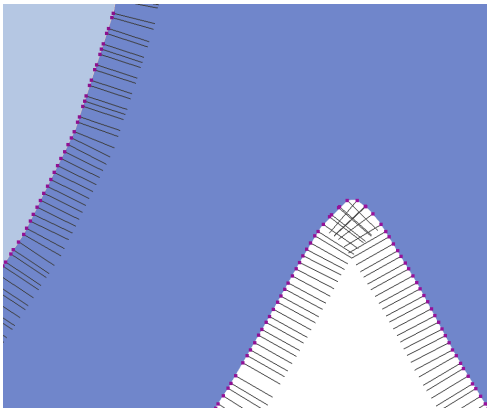

Figure 6: Part of the mesh with its boundary tracking particles. Normals are shown.

5. Simplify the segment list.

For the last step, a straightforward linear complexity ($O(n_{\text{nodes}})$) algorithm is applied by using the node-segment connectivity. The most difficult part is to find the suitable set of neighbors. If too large time steps are used, the FE solution becomes unstable, and the interpolated velocities for updating the particles leaves the topology in bad shape where there is little hope to construct a meaningful mesh. Fine tuning of the discretization parameters in GBPM is required to obtain a well defined surface for remeshing.

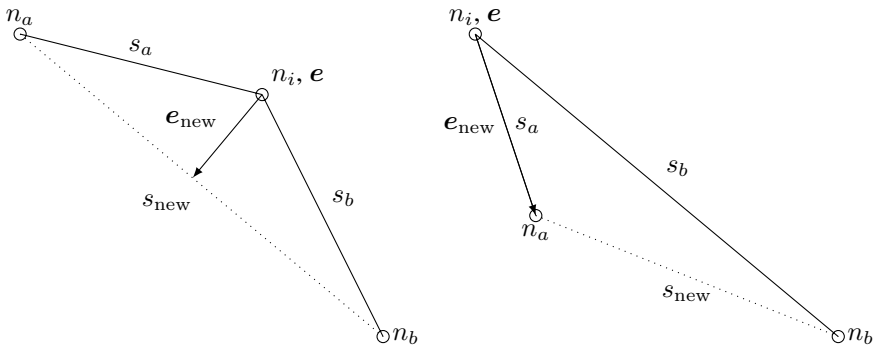

Figure 7: Illustration of the accumulated error when removing a node in a polygon. Two different cases are shown where n_i is checked for potential removal.

Algorithm 1 PSLG simplification algorithm

Construct the node-segments mapping; $c_i : n_i \mapsto [s_j]$
for all n_i **do**
  if $\#c_i = 2$ **then**
    $e_{\text{new}} \leftarrow \|\boldsymbol{e}_{\text{new}}\|$
    $e \leftarrow |(\boldsymbol{e} + \boldsymbol{e}_{\text{new}}) \cdot \boldsymbol{e}|/\|\boldsymbol{e}\|$
    if $\max(e_{\text{old}}, e_{\text{new}}) \leq d$ **then**
      Delete node n_i
      Delete edges s_a and s_b
      Add edge s_{new}
      $\boldsymbol{e}_a \leftarrow \boldsymbol{e}_a + \boldsymbol{e} + \boldsymbol{e}_{\text{new}}$
      $\boldsymbol{e}_b \leftarrow \boldsymbol{e}_b + \boldsymbol{e} + \boldsymbol{e}_{\text{new}}$
    end if
  end if
end for

The basic algorithm for removal of nodes and edges is described in Algorithm 1 with the accompanying illustration in Figure 7. This algorithm is conservative in the sense that the deviation of the new path is never more than the specified limit d. It also preserves direction of the new segments, and runs in linear time for any list of nodes and segments with arbitrary connections (unsorted).

7 Numerical Examples

In the subsequent numerical examples, we shall adopt a linear model, by setting $t_* \to \infty$, whereby the material parameters are viscosity, μ, and surface energy, γ_{s}. Due to the linearity, the velocity will be directly proportional to $\frac{\gamma_{\mathrm{s}}}{\mu}$. These parameters are set to unit values in the following simulations, and the time steps are chosen sufficiently small in order to obtain stability when updating the geometry.

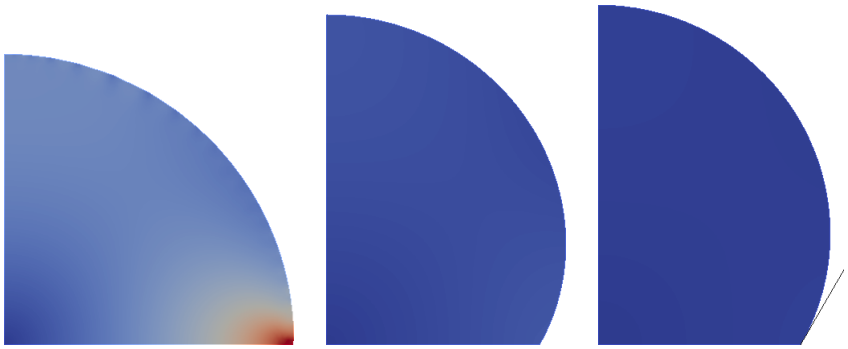

(a) $t = 0$ (b) $t = \frac{1}{2}t_{\mathrm{end}}$ (c) $t = t_{\mathrm{end}}$

Figure 8: Snapshots of droplet with vertical symmetry on a flat horizontal surface

In Figure 8 the contact angle for a droplet on a hard surface is computed using only the surface energy $\gamma_{\mathrm{s}} = 2$ for the curved boundary (Liquid-Gas (LG) interface) and $\gamma_{\mathrm{s}} = 1$ for the horizontal boundary (Liquid-Solid (LS) interface). In the equilibrium state the wetting angle corresponds to the analytical expression for a simple contact (the Young-Dupre equation);

$$0 = \gamma_{\mathrm{SG}} - \gamma_{\mathrm{SL}} - \gamma_{\mathrm{LG}} \cos(\theta) \tag{76}$$

where $\gamma_{\mathrm{LG}} = 2$ and $\gamma_{\mathrm{SL}} - \gamma_{\mathrm{SG}} = 1$. The analytical contact angle for this case is $\arccos(-\frac{1}{2}) = 120^\circ$ and is illustrated in Figure 8c with a black line. This holds for both rotational symmetry and extruded 2D.

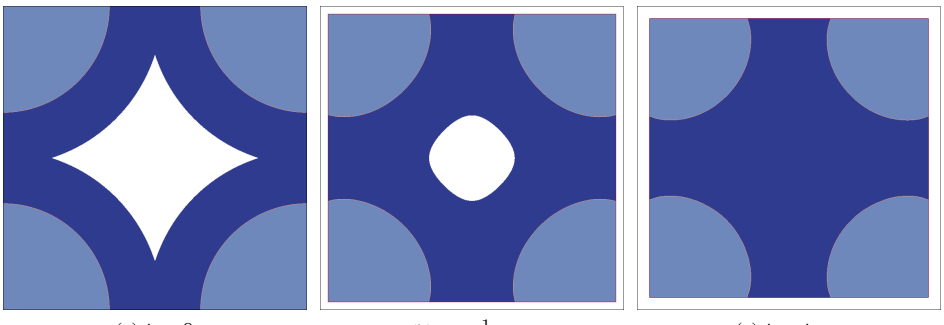

(a) $t = 0$ (b) $t = \frac{1}{2}t_{\mathrm{end}}$ (c) $t = t_{\mathrm{end}}$

Figure 9: Snapshots of computed RVE-configurations at selected times when subjected to free sintering defined by $\bar{\boldsymbol{\sigma}} = \mathbf{0}$

The first RVE-example, for which results are shown in Figure 9 to 11, represents free sintering in a given macroscopic point. All RVE simulations are performed with traditional Dirichlet boundary conditions. While microperiodic boundary conditions can be expected to yield better results, they are not used here due to the increased complexity in conjunction with remeshing. The porosity is not used in the calculations but is a post-processed value evaluated from the pore and particle areas. In Figure 11, the effect of the boundary conditions can be seen. For the 9-particles RVE, the effects of the boundary condition have vanished almost completely.

The second RVE-example, for which results are shown in Figures 12 and 13, represents a macroscopically rigid situation, i.e. fully constrained sintering. This is achieved by setting $\bar{\boldsymbol{d}} = \mathbf{0}$. Figure 13 shows that the homogenized mean stress, $\bar{\sigma}_{\mathrm{m}}$, which is taken as the driving force of the sintering process, can vary with the pore morphology by a factor larger than 2. The mean stress shown in Figure 13 and Figure 15 is normalized by the nominal sintering

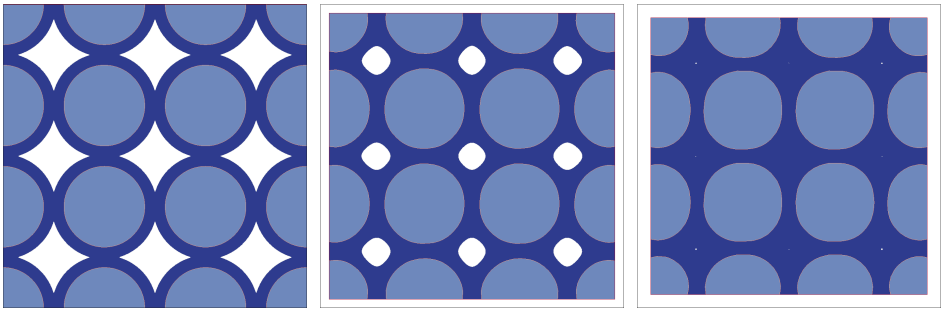

(a) $t = 0$ (b) $t = \frac{1}{2}t_{\text{end}}$ (c) $t = t_{\text{end}}$

Figure 10: Snapshots of computed RVE-configurations with 9 particles at selected times when subjected to free sintering defined by $\bar{\boldsymbol{\sigma}} = \mathbf{0}$

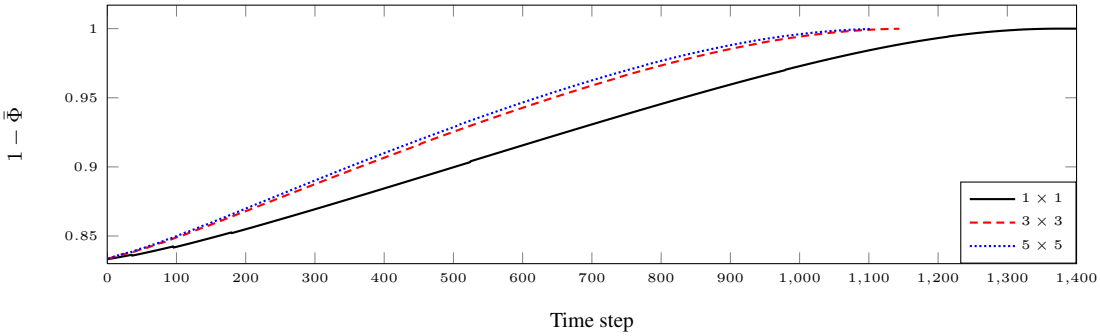

Figure 11: Evolution of porosity, $\bar{\Phi} \stackrel{\text{def}}{=} |\Omega_{\square}^{\text{pore}}|/|\Omega_{\square}|$, over time for free sintering defined by $\bar{\boldsymbol{\sigma}} = \mathbf{0}$

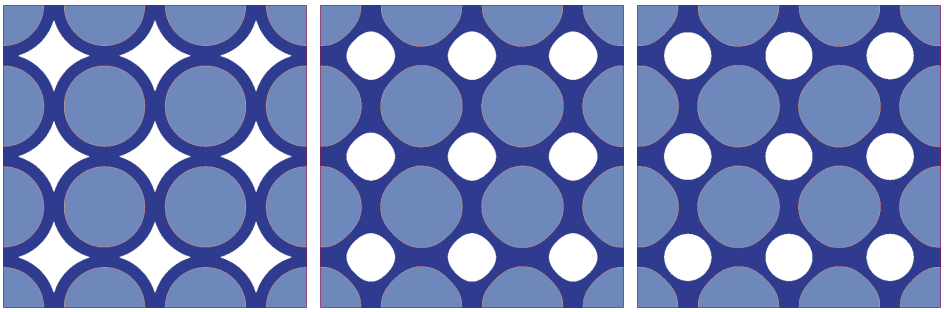

(a) $t = 0$ (b) $t = \frac{1}{2}t_{\text{end}}$ (c) $t = t_{\text{end}}$

Figure 12: Snapshots of computed RVE-configurations at selected times for a macroscopically rigid material defined by $\bar{\boldsymbol{d}} = \mathbf{0}$

stress (for a single pore) defined as

$$\sigma_{\text{sint}} \stackrel{\text{def}}{=} \frac{\gamma_{\text{s}}}{\sqrt{|\Omega_{\square}^{\text{pore}}|/\pi}} \tag{77}$$

where γ_{s} is the surface energy for the fluid-pore surface. This value is typically used in macroscale modeling when spherical pores are assumed, cf. Mähler and Runesson (2003).

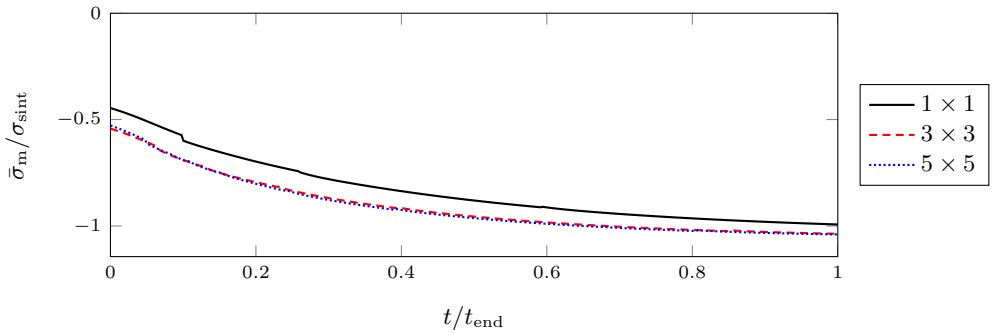

Figure 13: Evolution of the homogenized mean stress ($\bar{\sigma}_{\mathrm{m}} \overset{\mathrm{def}}{=} \frac{1}{3}\boldsymbol{I} : \bar{\boldsymbol{\sigma}}$) over time for a macroscopically rigid material defined by $\bar{\boldsymbol{d}} = \boldsymbol{0}$

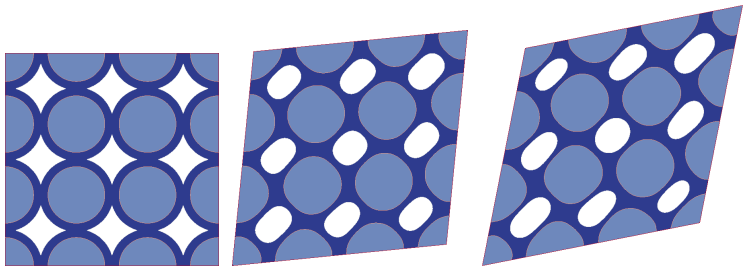

(a) $t = 0$ (b) $t = \frac{1}{2}t_{\mathrm{end}}$ (c) $t = t_{\mathrm{end}}$

Figure 14: Snapshots of computed RVE-configurations at selected times for constant macroscopic shear rate: $\bar{\boldsymbol{d}} = \bar{d}_{12}(\boldsymbol{e}_1 \otimes \boldsymbol{e}_2 + \boldsymbol{e}_2 \otimes \boldsymbol{e}_1)$

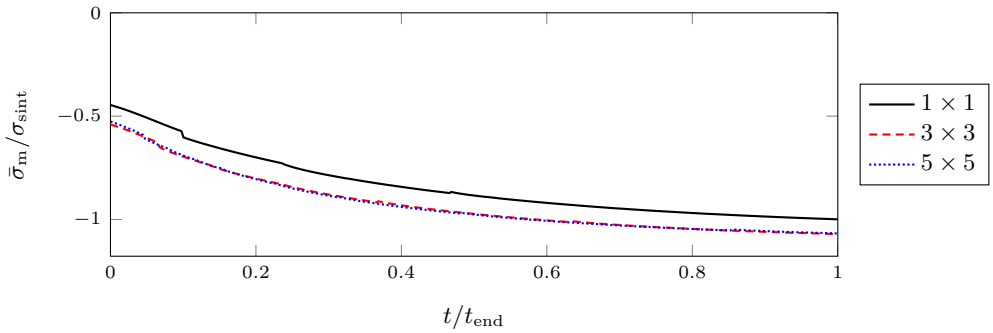

Figure 15: Evolution of the homogenized volumetric stress over time for constant macroscopic shear rate: $\bar{\boldsymbol{d}} = \bar{d}_{12}(\boldsymbol{e}_1 \otimes \boldsymbol{e}_2 + \boldsymbol{e}_2 \otimes \boldsymbol{e}_1)$

The final RVE-example, for which results are shown in Figures 14 and 15, represents a situation of macroscopic shear under isochoric conditions. The development of $\bar{\sigma}_{\mathrm{m}}$ in Figure 15 is similar to that in Figure 13 pertinent to the macroscopically rigid condition; hence, the superposed shear will result in only a small contribution to the mean stress (due to the elliptical shape of the pores). Here, we remark that t_{end} does not in any way represent a stationary state since the fluctuation field within the RVE is clearly non-homogeneous at the time t_{end}. It is therefore chosen equal to that of the equilibrium state for the macroscopically rigid RVE.

(a) Initial state

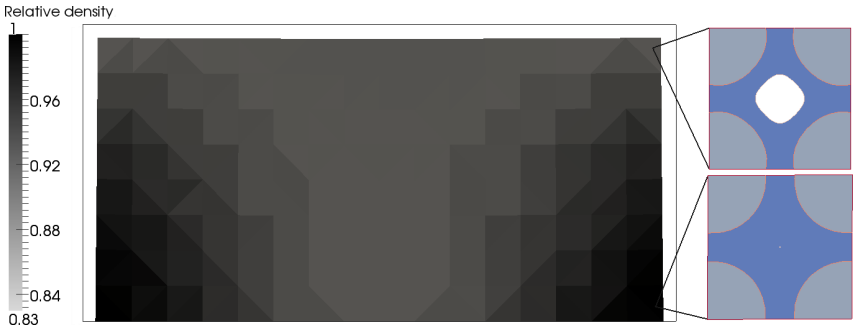

(b) End-of-simulation state

Figure 16: A fully coupled FE^2 simulation.

The final numerical example concerns a full-fledged FE^2 simulation of the sintering of a component with simple shape, whereby the relative density in the green body (initial distribution of relative density for the subsequent sintering analysis) is assumed to be inhomogeneous as shown in Figure 16a. In fact, it was assumed that the compaction gave somewhat larger relative density along the sides. A snapshot of the deformed shape and the relative density distribution at the final step of the simulation are shown in Figure 16b. Since the present formulation presumes a macroscopically compressible response, the simulation is stopped when the porosity first vanishes in any macroscopic integration point and this point becomes fully dense. This situation is achieved quite early, which is a serious restriction of the present modeling stage (see outlook below).

8 Conclusions and Outlook

In this paper we have presented a novel approach to simulate the sintering process as a problem of computational homogenization. Examples of the response of a single RVE subjected to different macroscopic conditions showed that the results converged quite rapidly with increasing RVE-size for the adopted Dirichlet boundary conditions. The final FE^2-analysis for an inhomogeneous initial distribution of the macroscopic porosity was carried out using a code parallelization with respect to the macroscale integration points.

The FE^2 algorithm has been implemented in the open source code OOFEM (cf. Patzák (2000)). All parts have been implemented with a modular approach, implying that they can be used individually and with other problems. These modules will be available in the future official releases of OOFEM and include Dirichlet prolongation boundary condition, Taylor-Hood elements for Stokes flow, surface tracking and meshing routines.

As to the future developments, the most pressing issue is that of dealing with macroscopic incompressibility. For this purpose, a mixed $\bar{\boldsymbol{v}}$-$\bar{p}$-format will be adopted. Among other issues of importance are the implementation of microperiodic and Neumann boundary conditions on the RVE and a statistical distribution of the microstructure characteristics. Above all, in order to make parameter identification meaningful of the subscale constituents, it is necessary to extend the geometric description to three dimensions.

References

Dettmer, W. G.; Perić, D.: A computational framework for free surface fluid flows accounting for surface tension. *Computer Methods in Applied Mechanics and Engineering*, 195, 23-24, (2006), 3038–3071.

Hughes, T. J. R.; Feijo, G. R.; Mazzei, L.; Quincy, J.-B.: The variational multiscale method - a paradigm for computational mechanics. *Computer Methods in Applied Mechanics and Engineering*, 166, 1-2, (1998), 3–24.

Jagota, A.; Dawson, P. R.: Micromechanical modeling of powder compacts — I. Unit problems for sintering and traction induced deformation. *Acta Metallurgica*, 36, 9, (1988a), 2551–2561.

Jagota, A.; Dawson, P. R.: Micromechanical modeling of powder compacts — II. Truss formulation of discrete packings. *Acta Metallurgica*, 36, 9, (1988b), 2563–2573.

Javili, A.; Steinmann, P.: A finite element framework for continua with boundary energies. Part I: The two-dimensional case. *Computer Methods in Applied Mechanics and Engineering*, 198, 27-29, (2009), 2198–2208.

Javili, A.; Steinmann, P.: A finite element framework for continua with boundary energies. Part II: The three-dimensional case. *Computer Methods in Applied Mechanics and Engineering*, 199, 9-12, (2010), 755–765.

Larson, M. G.; Må lqvist, A.: Adaptive variational multiscale methods based on a posteriori error estimation: Energy norm estimates for elliptic problems. *Computer Methods in Applied Mechanics and Engineering*, 196, 21-24, (2007), 2313–2324.

Larsson, F.; Runesson, K.: RVE computations with error control and adaptivity: the power of duality. *Computational Mechanics*, 39, 5, (2006), 647–661.

Leung, S.; Zhao, H.-K.: A grid based particle method for evolution of open curves and surfaces. *Journal of Computational Physics*, 228, 20, (2009a), 7706–7728.

Leung, S.; Zhao, H.-K.: A grid based particle method for moving interface problems. *Journal of Computational Physics*, 228, 8, (2009b), 2993–3024.

Lu, P.; Yi, W.; Xu, X.; German, R. M.: Porosity effect on densification and shape distortion in liquid phase sintering. *Materials Science and Engineering A*, 318, 1-2, (2001), 111–121.

Mähler, L.; Runesson, K.: Modelling of solid-phase sintering of hardmetal using a mesomechanics approach. *Mechanics of Cohesive-frictional Materials*, 5, 8, (2000), 653–671.

Mähler, L.; Runesson, K.: Constitutive Modeling of Cold Compaction and Sintering of Hardmetal. *Journal of Engineering Materials and Technology*, 125, 2, (2003), 191.

Patzák, B.: OOFEM project home page (2000).

Reid, C. R.; Oakberg, R. G.: A continuum theory for the mechanical response of materials to the thermodynamic stress of sintering. *Mechanics of Materials*, 10, 3, (1990), 203–213.

Saksono, P. H.; Perić, D.: On finite element modelling of surface tension: Variational formulation and applications – Part I: Quasistatic problems. *Computational Mechanics*, 38, 3, (2006a), 265–281.

Saksono, P. H.; Perić, D.: On finite element modelling of surface tension: Variational formulation and applications – Part II: Dynamic problems. *Computational Mechanics*, 38, 3, (2006b), 251–263.

Shewchuk, J. R.: Triangle: Engineering a 2D Quality Mesh Generator and Delaunay Triangulator. In: M. C. Lin; D. Manocha, eds., *Applied Computational Geometry: Towards Geometric Engineering*, vol. 1148 of *Lecture Notes in Computer Science*, pages 203–222, Springer Berlin / Heidelberg (May 1996).

Steinmann, P.: On boundary potential energies in deformational and configurational mechanics. *Journal of the Mechanics and Physics of Solids*, 56, 3, (2008), 772–800.

Svoboda, J.; Riedel, H.; Gaebel, R.: A model for liquid phase sintering. *Acta Materialia*, 44, 8, (1996), 3215–3226.

van de Vorst, G. A. L.: Integral method for a two-dimensional Stokes flow with shrinking holes applied to viscous sintering. *Journal of Fluid Mechanics*, 257, (1993), 667–689.

Xu, K.; Mehrabadi, M. M.: A micromechanical model for the initial rearrangement stage of liquid phase sintering. *Mechanics of Materials*, 25, 2, (1997), 157–137.

Zhou, H.; Derby, J. J.: Three-Dimensional Finite-Element Analysis of Viscous Sintering. *Journal of the American Ceramic Society*, 81, 3, (1998), 533–540.

Zhou, H.; Derby, J. J.: An assessment of a parallel, finite element method for three-dimensional, moving-boundary flows driven by capillarity for simulation of viscous sintering. *International Journal for Numerical Methods in Fluids*, 36, 7, (2001), 841–865.

Address: Mikael Öhman, Kenneth Runesson and Fredrik Larsson, Department of Applied Mechanics, Chalmers University of Technology, Hörsalsvägen 7B Gothenburg.
email: `mikael.ohman@; kenneth.runesson@; fredrik.larsson@chalmers.se.`